International Journal of Heat and Mass Transfer 136 (2019) 1199–1216

Contents lists available at ScienceDirect

International Journal of Heat and Mass Transfer

journal homepage: www.elsevier.com/locate/ijhmt

Experimental and computational investigation on two-phase flow and heat transfer of highly subcooled flow boiling in vertical upflow

Jeongmin Lee [a], Lucas E. O'Neill [a], Seunghyun Lee [b], Issam Mudawar [a,*]

[a] Purdue University Boiling and Two-Phase Flow Laboratory (PU-BTPFL), School of Mechanical Engineering, Purdue University, 585 Purdue Mall, West Lafayette, IN 47907, USA
[b] Gwangju Institute of Science and Technology Two-Phase Flow and Thermal Management Laboratory, School of Mechanical Engineering, 123 Cheomdangwagi-ro, Buk-gu, Gwangju 61005, South Korea

ARTICLE INFO

Article history:
Received 12 April 2018
Received in revised form 6 March 2019
Accepted 7 March 2019
Available online 20 March 2019

Keywords:
Two-phase flow
Subcooled flow boiling
CFD
Vertical upflow

ABSTRACT

This study explores subcooled nucleate flow boiling of FC-72 in a rectangular channel having two opposite heating walls at different mass velocities and wall heat fluxes ranging from 42% to 45% of CHF. Experiments are performed in which constant and equal heat fluxes are supplied from the heating walls, with local wall temperatures measured at several axial locations and used to determine axial variations of local heat transfer coefficient. Additionally, detailed information on flow pattern and phase distribution is captured by high-speed video through the channel's transparent sidewalls. Experimental values for key fluid flow and thermal parameters are compared to predictions of 2D computational simulations using ANSYS FLUENT. The computations are based on the multi-phase volume of fluid (VOF) model combined with an appropriate phase change model, and account for conjugate heat transfer along the heating walls. Computed transverse profiles and stream-wise variations of void fraction, flow velocity, and wall temperature are examined. The computed results show reasonable agreement with experimentally captured interfacial behavior as well as heat transfer parameters. Computed cross-sectional temperature profiles for the mixture show non-equilibrium subcooled boiling with steep temperature gradients near the heating walls and low temperature liquid in the core region. This study is concluded by exploring limitations of the 2D model used.

1. Introduction

1.1. Emergence of two-phase thermal management schemes

For many decades, single-phase cooling methods, using air or liquid, have dominated a vast number of industrial applications. Because of relatively low to moderate heat fluxes encountered in these applications, single-phase methods have satisfied cooling demands while maintaining acceptable temperatures of heat dissipating surfaces. As heat loads continued to increase, however, efforts became focused on improving heat conduction and convection by enhancing coolant thermal conductivity [1,2], modifying flow geometry [3,4], and better optimizing cooling system design [5]. Despite these advances, developments in many industries have resulted in unprecedented escalation in heat load from relatively compact system packages, especially in more recent electronic and power applications, including electronic data centers, hybrid vehicle power electronics, aircraft and spacecraft avionics, X-ray medical devices, advanced radar, and directed energy laser and microwave electronics [6,7]. Increased heat fluxes and high sensitivity to operating temperature are strong evidence single-phase schemes can no longer fulfill cooling requirements.

To cope with these trends, interest has recently shifted to use of two-phase thermal management schemes where device heat is acquired by boiling and rejected by condensation. These two-phase schemes provide improved heat transfer coefficients, which is rooted in their ability to utilize the coolant's both sensible and latent heat. In most of these systems, boiling is used to dissipate the heat from high-flux surfaces, and the liquid-vapor mixture is routed to a condenser, wherein the heat is rejected to the ambient, returning the vapor to liquid state.

With intense interest in two-phase systems came an urgent need to develop accurate and robust predictive design tools. Key among design parameters crucial to implementation of two-phase thermal management systems are pressure drop, heat transfer coefficient, and, most importantly, critical heat flux (CHF). Exceeding CHF amounts to catastrophic failure of the heat-dissipating device, as it triggers unsteady and often drastic

* Corresponding author.
E-mail address: mudawar@ecn.purdue.edu (I. Mudawar).
URL: https://engineering.purdue.edu/BTPFL (I. Mudawar).

https://doi.org/10.1016/j.ijheatmasstransfer.2019.03.046
0017-9310/

Nomenclature

c_p	specific heat at constant pressure
Δc	mesh (cell) size
E	energy per unit mass
e	parameter in Smith model
F	force per unit volume
G	mass velocity
g	gravitational acceleration
H	larger width of flow channel's cross-section
h	heat transfer coefficient
H_a	heated wall *a*
H_b	heated wall *b*
h_{fg}	latent heat of vaporization
I	turbulent intensity
k	thermal conductivity
k_{eff}	effective thermal conductivity
L_d	upstream development length of flow channel
L_e	exit length of flow channel
$L_{e,c}$	added exit length in computational domain
L_h	heated length of flow channel
$\dot{m}$	volumetric mass source (kg/s·m^3)
q''	wall heat flux
Re_D	Reynolds number based on hydraulic diameter
r_i	mass transfer intensity factor
S	slip ratio
S_h	volumetric energy source (W/m^3)
T	temperature
t	time
Δt	time-step size
T_{in}	temperature at channel inlet
t_s	thickness of solid wall in computational domain
T_{sat}	saturation temperature
u	velocity
u'	turbulent velocity fluctuation
u_τ	friction velocity
W	smaller width of flow channel's cross-section
x	vapor quality
x_d	thermodynamic equilibrium quality at net vapor generation point
x_e	thermodynamic equilibrium quality
y	distance perpendicular to the wall
y^+	dimensionless distance perpendicular to the wall
z	stream-wise coordinate from inlet to heated portion of flow channel

Greek symbols

α	volume fraction; void fraction
μ	dynamic viscosity
ν	kinematic viscosity
ρ	density
σ	surface tension
ϕ	property

Superscripts

T	transpose

Subscripts

f	liquid
g	vapor
i	index for phase
in	inlet to heated portion of flow channel
sat	saturation
wall	wall

increase in device temperature, which may lead to device overheating or physical burnout. This explains the emphasis that has been placed on CHF prediction [8–13].

Another challenge to the development of two-phase thermal management systems is the large variety of possible boiling configurations, the choice of which being highly dependent on operational environment. They include several schemes that have been target of studies at the Purdue University Boiling and Two-Phase Flow Laboratory (PU-BTPFL) and other organizations, and include pool boiling [14–16], falling film [17,18], macro-channel [19] and micro-channel [20–22] flow boiling, spray cooling [23–25], and jet impingement [26–28], as well as hybrid cooling schemes [29].

1.2. Mechanisms and predictive methods for subcooled flow boiling in channels

The present study concerns two-phase flow and heat transfer characteristics along a channel into which liquid coolant is supplied in subcooled state (well below saturation temperature). A key heat transfer merit of subcooled boiling is ability to capitalize upon relatively large sensible heat content in addition to latent heat to achieve superior heat transfer performance. Another merit is its ability to maintain low void fraction along the flow channel, especially at high mass velocities, which both prevents escalation in pressure drop commonly encountered in most flow boiling systems, and delays the onset of CHF. Despite these important attributes, heat transfer mechanisms of subcooled flow boiling are less fully understood than those of saturated flow boiling. Much of the difficulty in modeling subcooled boiling stems from high non-equilibrium between the liquid and vapor phases.

Extensive research efforts have focused on measuring and predicting key transitional parameters of subcooled flow boiling, including onset of nucleate boiling (ONB) [30,31], onset of significant void (OSV) [32–34], and onset of flow instability (OFI) [35,36]. Other important aspects are variations of both wall temperature and heat transfer coefficient along the channel. Key to understanding these spatial variations is relating heat transfer characteristics to development of the near-wall bubble layer along the heated wall, which is often far too thin in subcooled flow to capture experimentally with sufficient resolution. Gradual axial development of this layer by combination of bubble growth and coalescence may also culminate in a fairly continuous vapor layer along the downstream regions of the channel wall, which is a precursor to CHF [11].

In general, subcooled flow boiling is initiated with a single-phase liquid region at the channel inlet. Gradual warming of liquid along the channel wall causes the wall to exceed saturation temperature, triggering bubble formation at ONB. With the bulk liquid well below saturation temperature, the bubbles incur appreciable condensation, which greatly limits penetration of the bubble layer into the bulk (core) region. As bulk liquid farther downstream gets warmer, condensation is suppressed, and bubble layer growth leads to OSV, which is accompanied by observable penetration into the bulk flow. Depending on combination of channel hydraulic diameter and length, inlet pressure, inlet quality, mass velocity, and heat flux, the bubble layer may exhibit significance coalescence and growth downstream, and the boiling flow may even transition from subcooled to saturated.

Investigators have employed several methods to predict heat transfer behavior in subcooled flow boiling. They include purely

empirical correlations with relatively narrow application range, analytical (including semi-empirical) models, and computational models. Recently, another method that has gained popularity for design of two-phase thermal management systems is use of 'universal correlations' (*e.g.,* [37–39]), which rely on massive databases obtained from many sources for large variety of fluids, and which encompass broad variations of inlet pressure, inlet quality, mass velocity, channel diameter, channel length, and wall heat flux.

1.3. Predictions of two-phase flow and heat transfer using computational methods

Starting in the 1980s, computational methods have shown unprecedented success in predicting single-phase fluid flow and heat transfer, evidenced by good agreement with experimental data for a broad variety of flow configurations. Over time, significant improvements have been made to single-phase predictions using a variety of commercial software packages, and, with greatly enhanced computation speed, these tools are becoming increasingly more user friendly and more robust.

Compared to single-phase flows, however, computing tools have lagged significantly behind in their ability to predict two-phase flow, especially in the presence of phase-change. While computing tools have lessened reliance on empirical correlations and costly experimental work for single-phase applications, the same cannot be said of two-phase applications. As indicated in a recent review article by Kharangate and Mudawar [40], successes in computational modeling of two-phase flows have thus far been limited to simple configurations such as pool boiling and single droplet impact on heated walls. Another important limitation of most two-phase computing tools is unusually long computing time, and reliance on high performance computing resources even when tackling relatively simple two-phase configurations. For example, computational flow boiling studies have been limited mostly to modeling a single bubble or few bubbles, showing some successes in capturing bubble growth, deformation, and rise, as well as flow field around the bubble [41–43]. But the same modeling tools are not yet capable of predicting growth, coalescence, and/or breakup of a large number of bubbles in more realistic flow boiling situations.

Given the complexity of phase change mechanisms encountered in many modern applications, there is an urgent need to greatly enhance the capabilities of computing tools to tackle relevant phenomena. This includes important interfacial dynamics and heat transfer phenomena such as bubble growth, departure and coalescence, interfacial waviness, and turbulence, as well as ability to predict ONB and CHF, especially for complicated flow geometries. As suggested by Kharangate and Mudawar, several important research tasks must be undertaken before investigators can achieve the long-term objective of developing a unified, physically based, accurate, and computationally efficient methodology.

Two main challenges to improving the effectiveness of two-phase computational models are accurate interfacial tracking and phase change modeling. Two popular approaches to modeling two-phase flows are the Lagrangian and Eulerian methods. By employing boundary-fitted grids, the former provides high accuracy in interface capture by solving governing equations separately for each phase and matching interfacial conditions iteratively. But, because of very fine mesh size, Lagrangian methods require considerable computing time, which is why they have been applied only to very basic two-phase configurations.

The most popular of Eulerian methods to track liquid-gas or liquid-vapor interfaces are the Level-Set (LS) method [44] and Volume-of-Fluid (VOF) method [45]. Of the two, the LS method provides superior capture of curvature and sharp interfaces, but suffers numerical issues associated with instability in mass conservation when tackling two-phase flows with phase change. The VOF method involves tracking the interface using phase volume fraction inside a cell, and, while it is less accurate in predicting interface topography than LS, it is comparatively simpler, less time-consuming, and more accurate in tackling mass conservation. The shortcomings in predicting interface topography with the VOF method are reduced with application of a geometric-reconstruction (piecewise-linear) scheme. This is the reason the present study will utilize the VOF method with piecewise-linear scheme.

Recent literature has included several studies involving use of the VOF method to model two-phase flow situations with heat transfer. For example, Da Riva and Del Col [46] and Bortolin et al. [47] used the VOF method in 3D simulations of condensation along a mini-channel and showed good agreement with experimental results. Lee et al. [48] and Kharangate et al. [49] also used the VOF method to simulate 2D axisymmetric condensation along a vertical tube. Yang et al. [50] adopted the VOF method to simulate different flow regimes (bubbly, churn, slug, stratified, annular, and mist) in complicated geometries. Other flow boiling simulations involving a variety of boundary conditions (*e.g.,* uniform and non-uniform heat flux, conjugate heat transfer) [51–54] have also been undertaken and show reasonable predictions.

1.4. Objectives of study

This work is part of a collaborative effort between PU-BTPFL and NASA Glenn Research Center (GRC) to develop the Flow Boiling and Condensation Experiment (FBCE) for the International Space Station (ISS) [55,56]. The primary goals of this ISS facility will be to obtain long-duration flow boiling and flow condensation data in reduced gravity, which will later be used to develop empirical, analytical, and computational predictive tools for pressure drop and heat transfer associated with flow boiling and condensation in straight channels. The present study concerns the flow boiling portion of FBCE, and aims to provide a foundation for computational prediction of flow boiling with subcooled inlet conditions. Video records from prior experiments at PU-BTPFL, conducted in both Earth gravity [11,12,57–63] and microgravity [64,65], provide overwhelming evidence of bubble coalescence promoting the formation of a wavy vapor layer along the heated wall. This layer acts as precursor to CHF, which is arguably the most important design and safety parameter for most terrestrial and space applications involving heat flux controlled surfaces.

The present study will address the fluid flow and heat transfer characteristics for vertical upflow boiling of FC-72 in a rectangular channel, including initiation of the wavy vapor layer. Conditions for three mass velocities and different wall heat fluxes are examined both experimentally and computationally. Measured bubble size and vapor void fraction are used to validate the phase change model incorporated in the computational analysis. Choice of vertical upflow orientation is based on its ability to ensure flow symmetry for a channel that is heated along two opposite sides, in addition to its popularity in many engineering applications. Temporal and spatial averaging methods are employed to predict both the wall temperature and heat transfer coefficient. Aside from validating the model predictions against experimental measurements, this study will explore computationally important characteristics of flow boiling including void fraction, slip ratio, and velocity and temperature distributions, both across and along the flow channel.

2. Experimental methods

The present work is primarily computational in nature, but, to offer careful assessment of the ability of the computational scheme to accurately represent the physical processes in play, comparisons

with experimental results are also provided. Towards this end, a brief overview of experimental methods used to gather data presented herein is provided below.

The test section used in the present set of experiments is the Flow Boiling Module (FBM), part of NASA's ongoing Flow Boiling and Condensation Experiment (FBCE). The module is constructed by clamping three polycarbonate plates between two aluminum support plates, with the central polycarbonate plate having a portion milled out to create a flow channel. The central plate is then polished to optical grade, allowing flow visualization images to be captured through the channel's adiabatic sidewalls.

Fig. 1(a) provides schematics of the 2.5-mm by 5-mm flow channel milled into the central polycarbonate plate, which possesses a 327.9-mm development length (downstream of a honeycomb flow straightener), a 114.6-mm heated length, and a 60.9-mm exit length. The heated length features two oxygen-free copper slabs recessed into opposite walls with six resistive heaters connected electrically in parallel on the back of each.

Fig. 1(b) shows photos of the FBM with key features identified. Of particular note are the inlet and outlet fluid type-E thermocouples (inserted directly into the flow), opposite heated wall thermocouples (seven of which embedded into each heated wall between and on either end of the resistive heaters), and five pressure measurement points, with three corresponding to adiabatic measurement points and two used to measure pressure drop over the heated length.

The flow loop used to supply the working fluid, dielectric FC-72, to the FBM and control inlet conditions is depicted schematically in Fig. 1(c) and a photo with key components labeled is shown in Fig. 1(d). The loop consists of an Ismatech MCP-z magnetically coupled gear pump to circulate the working fluid, which first enters a filter to remove any particulates before passing through a turbine flow meter for flow rate measurement. Downstream of the flow meter, the fluid enters a bulk heater, with power supplied by a variac used to control thermodynamic conditions at the inlet of the FBM. Upon leaving the bulk heater, the fluid enters the FBM, which is mounted on a rotating platform to allow tests in multiple orientations; only results gathered in vertical upflow are examined in the present study. Electrical power supplied to heated walls of the flow channel is provided by the FBM heater control module and measured using current transducers. Exiting the FBM, the fluid passes through an air-cooled condenser to return the flow to single-phase liquid state. It then continues past an accumulator, which is included to allow for fluid volume changes resulting from phase change, before returning to the pump.

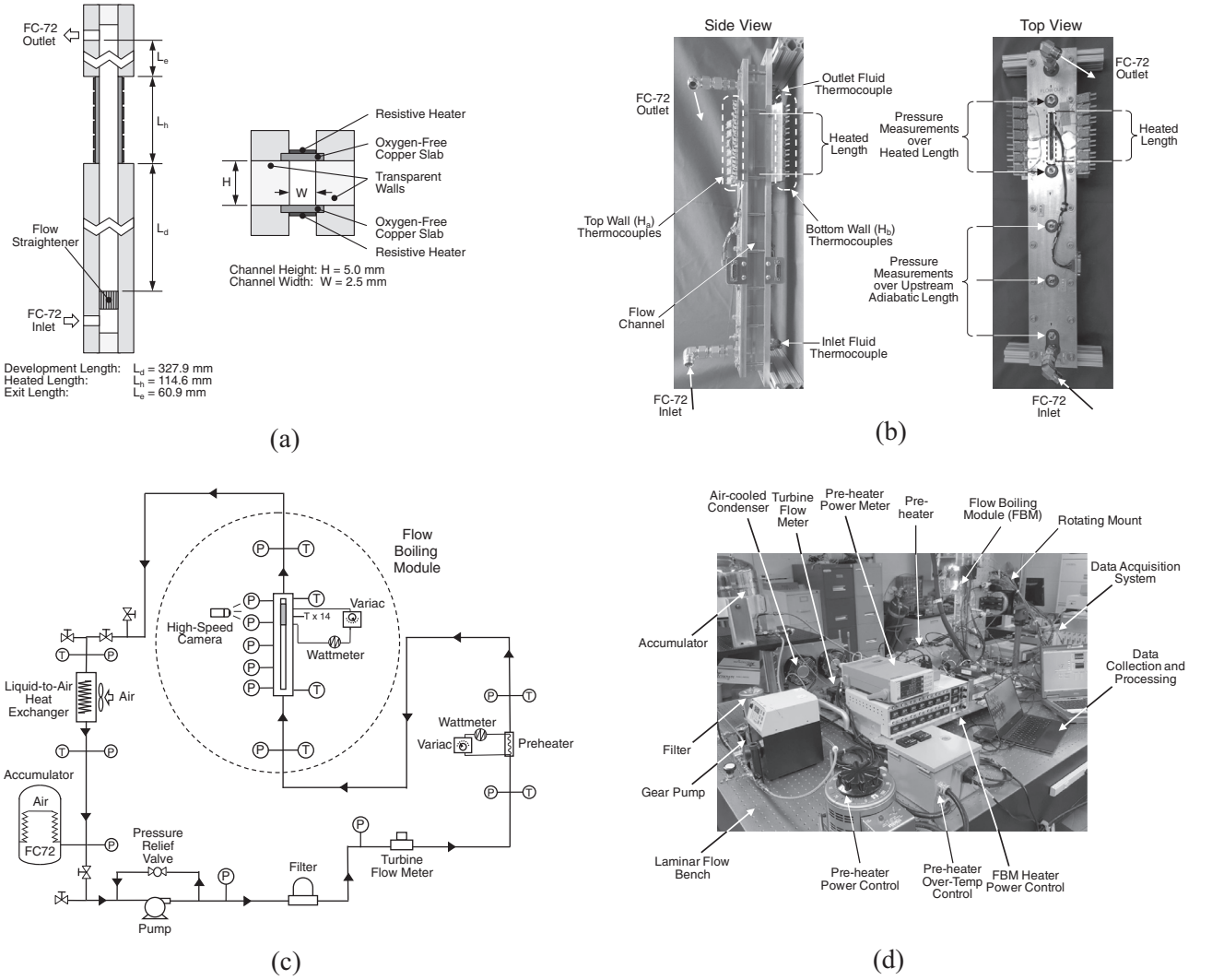

Fig. 1. (a) Schematics and (b) images of Flow Boiling Module (FBM) with key features identified, and (c) schematic and (d) images of experimental facility with key components labeled.

Data from pressure, temperature, flow rate, and power measurements throughout the system are obtained using an NI SCXI-1000 data acquisition system controlled by a LabVIEW code. Images are captured at a rate of 2000 frames per second (fps) with a pixel resolution of 2040 × 174 covering the entire 114.6-mm heated length of the channel. Illumination is provided from the opposite sides of the flow channel using blue LEDs, passing through a light shaping diffuser (LSD) to enhance illumination uniformity.

Type-E thermocouples with an accuracy of ±0.5 °C are used to measure fluid and heated wall temperatures throughout the system. Pressure measurements are made using transducers with an accuracy of ±0.1% and pressure drop accuracy of ±0.2%. The turbine flow meter has an accuracy of ±0.1%, and wall heat input is measured with an accuracy of ±0.5 W. Overall uncertainty in determining the heat transfer coefficient is ±8%.

For additional details on fluid components used, measurement techniques employed, and operating conditions tested, the reader is advised to consult a prior experimental study [66].

3. Numerical methods

3.1. Mathematical representation and numerical details

The present study employs the transient VOF method in ANSYS FLUENT for tracking interfacial behavior during flow boiling and accounting for mass transfer between the two phases. In the VOF model, volume fractions of each phase in a cell are calculated. Volume fraction is numerically defined as fraction of each phase occupying a cell, and the sum of volume fractions for the two phases is always equal to unity. It is assumed that the flow is incompressible, so density variations are not considered. Tracking of interface throughout the computational domain is accomplished by solving continuity equation for volume fraction [67].

For liquid phase,

$$\frac{\partial \alpha_f}{\partial t} + \nabla \cdot \left(\alpha_f \vec{u}_f\right) = \frac{1}{\rho_f} \sum \left(\dot{m}_{gf} - \dot{m}_{fg}\right), \tag{1}$$

and vapor phase,

$$\frac{\partial \alpha_g}{\partial t} + \nabla \cdot \left(\alpha_g \vec{u}_g\right) = \frac{1}{\rho_g} \sum \left(\dot{m}_{fg} - \dot{m}_{gf}\right), \tag{2}$$

where α_f, α_g, $\vec{u}_f$, $\vec{u}_g$, $\dot{m}_{gf}$, and $\dot{m}_{fg}$ are, respectively, volume fraction of liquid, volume fraction of vapor, liquid velocity, vapor velocity, mass transfer from vapor to liquid, and mass transfer from liquid to vapor.

The combined phase momentum and energy equations are given by

$$\frac{\partial}{\partial t}\left(\rho \vec{u}\right) + \nabla \cdot \left(\rho \vec{u}\,\vec{u}\right) = -\nabla P + \nabla \cdot \left[\mu\left(\nabla \vec{u} + \nabla \vec{u}^{T}\right)\right] + \vec{F}, \tag{3}$$

and

$$\frac{\partial}{\partial t}(\rho E) + \nabla \cdot \left(\vec{u}(\rho E + P)\right) = \nabla \cdot \left(k_{eff} \nabla T\right) + S_h, \tag{4}$$

where E (J/kg) is energy per mass. In the above equations, ρ, μ, and k_{eff}, are density, dynamic viscosity, and effective thermal conductivity, which are determined according to

$$\phi = \sum \alpha_i \phi_i, \tag{5}$$

where ϕ is the property being evaluated using a phase-weighted average of its liquid and vapor values. Implicit body force formulation is used since it is important for detachment of vapor and replenishment of liquid into the wall region. Surface tension force ($\vec{F}$) with wall adhesion is modeled using the Continuum Surface Force (CSF) method proposed by Brackbill [68]. The extra heat transfer involved in boiling and condensation is accounted for with a source term in the energy equation by multiplying the rate of mass transfer and latent heat,

$$S_h = h_{fg}\dot{m}. \tag{6}$$

To account for turbulence effects, the two-equation Shear-Stress Transport (SST) k-ω turbulence model with a turbulence damping factor of 10 is used. The alternative k-ε model was avoided due to its tendency to produce appreciable disturbances to interfacial temperature, with temperatures dropping below T_{sat} when employing low mass transfer intensity factor in the phase change model [48]. Also used in the present analysis is Low-Reynolds-Number correction for turbulent viscosity damping.

3.2. Computational domain and grid independence test

The computational geometry of the problem examined in this study is illustrated in Fig. 2. It consists of a two-dimensional flow channel with 5-mm × 144.6-mm fluid region, and two 1.04-mm × 114.6-mm solid walls. Here, actual dimensions of the experimental flow boiling module are used, excepting length of the fluid domain, which 30-mm longer than the heated length of the experimental module to prevent any outlet effects. This added fluid length is adiabatic, and does not include solid meshes through which thermal energy can be transferred. The computational domain includes two 1.04-mm thick solid meshes representing the copper heating walls, which allow for analysis of conjugate heat transfer from solid to fluid. A quadrilateral mesh is adopted for the entire domain. The mesh is non-uniform, gradually refined toward the walls to capture very small bubbles, as well as accurately account for fluid interactions in the viscous sublayers. The mesh is generated by ANSYS ICEM CFD [69], with additional mesh refinement conducted in ANSYS FLUENT.

Grid independence testing is conducted for a test case corresponding to an intermediate mass velocity of G = 836.64 kg/m^2 s. Five mesh types with different cell size near the wall are

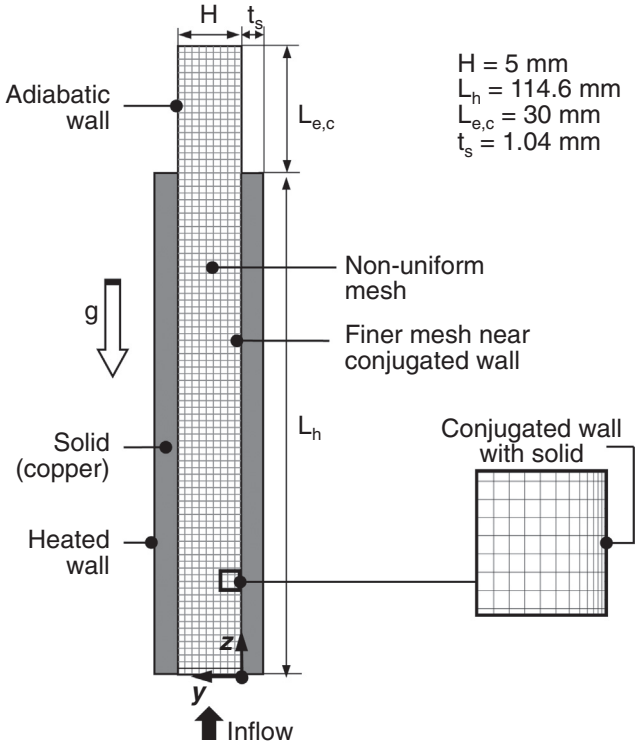

Fig. 2. Schematic of computational domain.

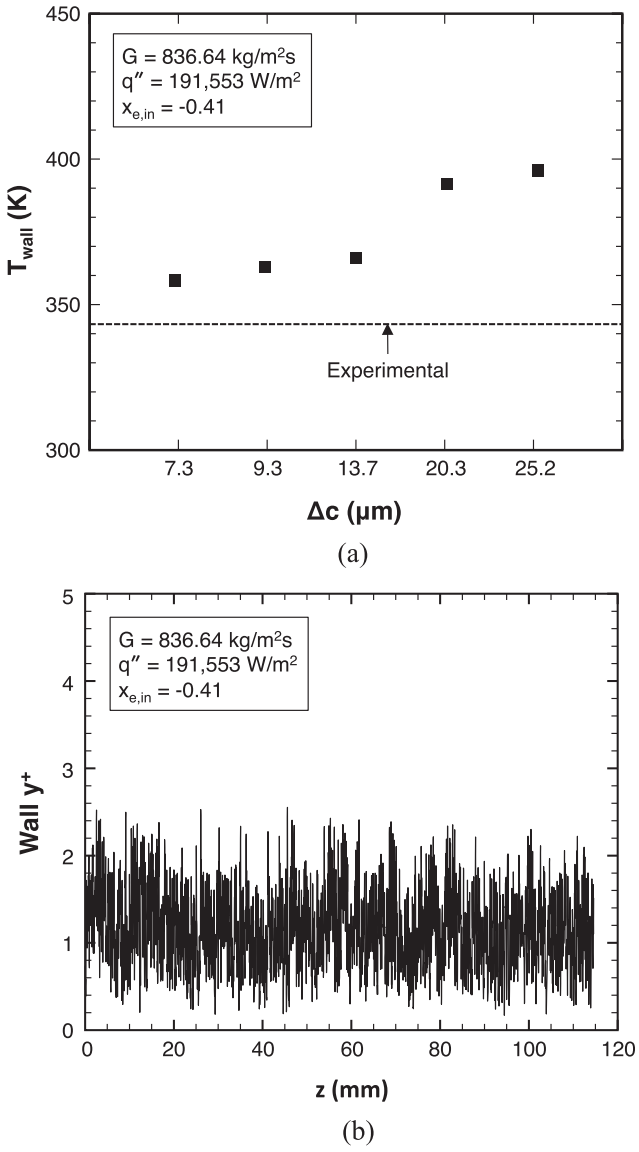

Fig. 3. (a) Grid independent test based on spatially time-averaged wall temperature. (b) Variation of y^+ along heated length for test case with intermediate mass velocity.

constructed, and spatially averaged wall temperature at each measurement point (z = 5.4, 22.7, 40, 57.3, 74.6, 91.9, and 109.2 mm) is computed after steady-state is reached, and compared with experimental data. Fig. 3(a) shows that asymptotic convergence of averaged wall temperature is achieved for near-wall cell size below about 14 μm. In this study, a cell size of Δc = 60 μm is used in the bulk flow region, with a minimum of Δc = 4 μm near the wall. It is important in turbulence modeling to determine suitable cell size near wall using non-dimensional distance y+ from the wall, which is defined as

$$y^+ = \frac{yu_\tau}{\nu}, \tag{7}$$

where y, u_τ, and ν are, respectively, distance from the wall, friction velocity, and kinematic viscosity. This parameter is used to describe how coarse or fine a mesh should be for the relevant flow pattern. In addition, capturing heat transfer with fluid interaction in the viscous sublayer is essential to predicting phase change. As shown in Fig. 3(b), the smaller cell size yields $y^+ < 5$ along the heated wall, which provides adequate resolution in capturing fluid interactions in the viscous sublayer. As indicated by Eq. (5), local properties, namely density and viscosity, which are used to define friction velocity and y+, are computed using a phase-weighted average of liquid and vapor content using void fraction, α. Because of phase change along the channel, local value of volume of fluid (void fraction), and, therefore, values of both friction velocity and y+, fluctuate along the channel.

3.3. Initial and boundary conditions

In this study, three different mass velocities and different wall heat fluxes are considered. As shown in Fig. 2, the computational domain does not include the adiabatic development length upstream of the heated portion of the channel. Instead, fully developed velocity profile and accompanying turbulent properties are employed in the inlet to the heated section. Turbulent intensity for the inlet boundary of each single-phase case is estimated from the empirical correlation for pipe flow [70]

$$I = \frac{u'}{\bar{u}} = 0.16 Re_D^{-1/8}. \tag{8}$$

No-slip boundary conditions are applied to the solid walls for which roughness height, roughness constant, and contact angle are set to 0 m, 0.5, and 5°, respectively.

Table 1 provides operating conditions and thermophysical properties used in the analysis. They include mass velocities of G = 445.8, 836.6, and 2432.5 kg/m^2 s with inlet temperatures of T_{in} = 300.97, 304.54, and 309.02 K and wall heat flux of q'' = 146,301, 191,553, and 194,873 W/m^2 (corresponding to ~42–45% of CHF), respectively, which are identical to those measured experimentally. Properties of FC-72 for each case are saturated values calculated at the measured inlet pressure. All cases considered correspond to subcooled inlet conditions, and, according to experimental data, specific pressure values are employed to the outlet boundary. For numerical stability, the global Courant number ($u\Delta t/\Delta c$) and time-step size are set to less than 0.7 and 8×10^{-6} s, respectively. Table 2 provides details of the numerical schemes adopted in the computations.

3.4. Phase change model

Using an appropriate phase change model is paramount to the ability to achieve accurate predictions of heat and mass transfer. A few popular models, including those by Schrage [70], Tanasawa [71], and Lee [72], were considered at first. Schrage's is a physics-based model developed from kinetic theory of gases, and

Table 1
Mass velocities for three cases examined with computational model and corresponding thermophysical properties used.

G (kg/m^2 s)	T_{sat} (K)	h_{fg} (J/kg mol)	ρ_f (kg/m^3)	$c_{p,f}$ (J/kg·K)	k_f (W/m·K)	μ_f (kg/m·s)	ρ_g (kg/m^3)	$c_{p,g}$ (J/kg·K)	k_g (W/m·K)	μ_g (kg/m·s)	σ (N/m)
Case 1 445.75	333.31	2.7608×10^7	1605.2	1120.1	0.0534	3.786×10^{-4}	16.591	946.91	0.0143	1.215×10^{-5}	0.0079
Case 2 836.64	335.35	2.9744×10^7	1608.2	1117.6	0.0536	3.846×10^{-4}	15.992	942.87	0.0142	1.210×10^{-5}	0.0080
Case 3 2432.51	342.52	2.7008×10^7	1589.6	1133.1	0.0527	3.497×10^{-4}	19.953	967.97	0.0149	1.243×10^{-5}	0.0073

Table 2
Numerical details and discretization methods.

Pressure-velocity coupling	Pressure-implicit with splitting of operators (PISO)
Gradient	Least squares cell based
Pressure	PRESTO!
Momentum	Third-order monotonic upstream-centered scheme for conservation laws (MUSCL)
Volume fraction	Geo-reconstruct
Turbulent kinetic energy	First-order upwind
Specific dissipation rate	First-order upwind
Energy	Second-order upwind
Transient formulation	First-order implicit

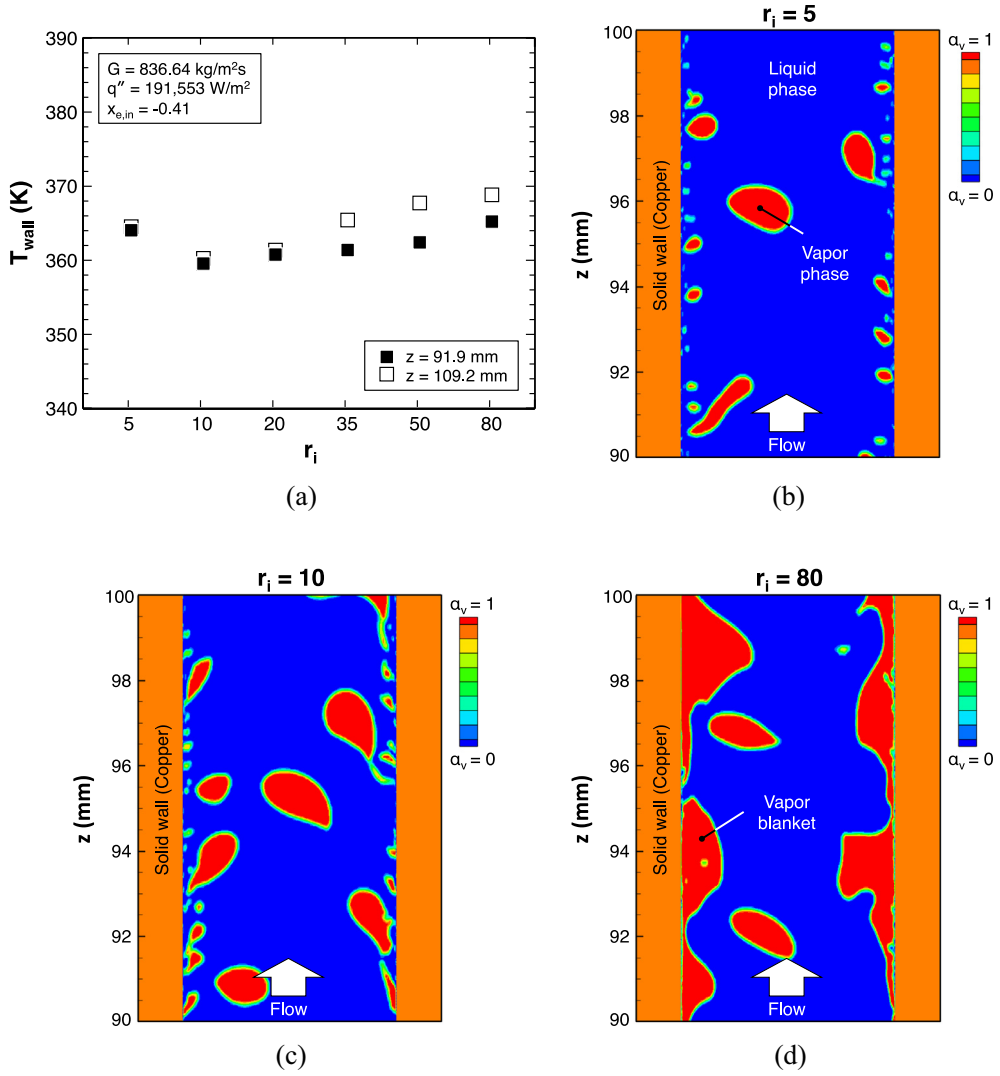

Fig. 4. (a) Variation of computed time-averaged wall temperature at two downstream locations of heated channel with r_i value, and predicted bubble behavior in the downstream region for (b) $r_i = 5$, (c) $r_i = 10$, and (d) $r_i = 80$.

considered generally quite accurate. However, it is not suitable for the present computations where only liquid initially occupies the entire channel, and phase change in Schrage's model requires existence of an interface between the two phases. Tanasawa's model is a modified form of the original Schrage model that accounts for small deviations of interface temperature from saturation temperature and assumes an interfacial mass flux linearly dependent on interface superheat. However, like the Schrage model, it is not applicable to this study since the present simulations starts from single-phase liquid, where no interface exists between the phases.

The Lee model, on the other hand, is quite effective at predicting phase change in the bulk flow at any location where fluid temperature exceeds saturation, allowing the model to predict spatial evolution of flow boiling along a channel from a single-phase liquid state at the inlet. The Lee model is therefore chosen for calculating mass transfer by phase change. The mass transfer rate per unit volume is given by

$$\dot{m}_{fg} = r_i \alpha_f \rho_f \frac{(T_f - T_{sat})}{T_{sat}} \text{ for evaporation } (T_f > T_{sat}) \tag{9a}$$

and

$$\dot{m}_{gf} = r_i \alpha_g \rho_g \frac{(T_{sat} - T_g)}{T_{sat}} \text{ for condensation } (T_g < T_{sat}), \quad (9b)$$

where r_i is an empirical coefficient called *mass transfer intensity factor*, different values of which can be assigned to different evaporation and condensation configurations. A major challenge when implementing the Lee model is assigning an appropriate value for r_i since this value can have a profound impact on wall temperature predictions. The value of r_i also influences all details of interfacial behavior (bubble diameters, interfacial area, and portion of one phase's molecules going to the surface of the other phase) along the flow channel. While the appropriate value for r_i in a given situation is generally not known in advance, an excessively high value for r_i can cause numerical convergence issues, while a very small r_i value can result in appreciable discrepancy between interfacial and saturation temperatures.

To determine an appropriate value for r_i for the present flow boiling configuration, several computational tests corresponding to intermediate values of mass velocity and wall heat flux of $G = 836.6$ kg/m^2 s and $q'' = 191{,}553$ W/m^2, respectively, are performed in which different values of r_i are attempted in pursuit of optimum value yielding good agreement between predictions and experiment. Fig. 4(a) shows the dependence of predicted time-averaged wall temperature at two axial locations ($z = 91.9$ and 109.2 mm) on r_i value, while Fig. 4(b)–(d) depict predicted bubble behavior along the heated portion of the channel for $r_i = 5$, 10, and 80, respectively. Notice that the wall temperature predictions in Fig. 4(a) correspond to the downstream region of the channel where Fig. 4(b)–(d) show the greatest sensitivity of bubble behavior to r_i value. Fig. 4(a) shows wall temperature decreases with increasing r_i down to $r_i = 10$ and gradually increases thereafter. This trend can be explained by the interfacial behavior depicted in Fig. 4(b)–(d). On one extreme, Fig. 4(b) shows $r_i = 5$ yields small overall vapor void fraction in the form of tiny wall bubbles, which is much smaller than the vapor behavior and void fractions observed experimentally. The behavior captured in this figure points to this low r_i value yielding predictions of heat removal from the wall by phase change that are comparatively quite small. On the other extreme, Fig. 4(d) shows $r_i = 80$ causes inordinate vapor growth and excessive bubble coalescence into a fairly continuous vapor blanket along the wall, conditions typically observed just before CHF and not at the heat flux used in the computations ($q'' = 191{,}553$ W/m^2), which is only 43.7% of measured CHF. The wall temperature trends in Fig. 4(a) are closely associated with the vapor void patterns depicted in Fig. 4(b)–(d). Below $r_i = 10$, a gradual increase in bubble generation at the wall with increasing r_i enhances heat transfer from the wall, which decreases wall temperature. On the other hand, increasing r_i value above $r_i = 10$ triggers gradual formation of an insulating vapor layer, which both compromises cooling effectiveness and increases wall temperature. Given that values below and above $r_i = 10$ produce interfacial behaviors different from those observed experimentally, all computations presented hereafter are performed using $r_i = 10$. Further validation of the effectiveness of this value will be provided later.

4. Results and discussion

4.1. Flow characteristics in subcooled boiling

4.1.1. Flow visualization results

Side-by-side experimental and computational visualizations of flow boiling along the entire heated length are depicted in Fig. 5 (a)–(c) for vertical upflow boiling with highly subcooled inlet conditions with $G = 445.8$, 836.6, and 2432.5 kg/m^2 s, respectively. Individual images in each sequence are $\Delta t = 10$ ms apart, which allows gradual temporal tracking of the interfacial behavior. Notice that the heat fluxes used with both the middle and high mass velocities and in both computations and experiment are fairly similar, however, a somewhat lower heat flux (31% of CHF) is used with the lowest mass velocity to also match available experimental results.

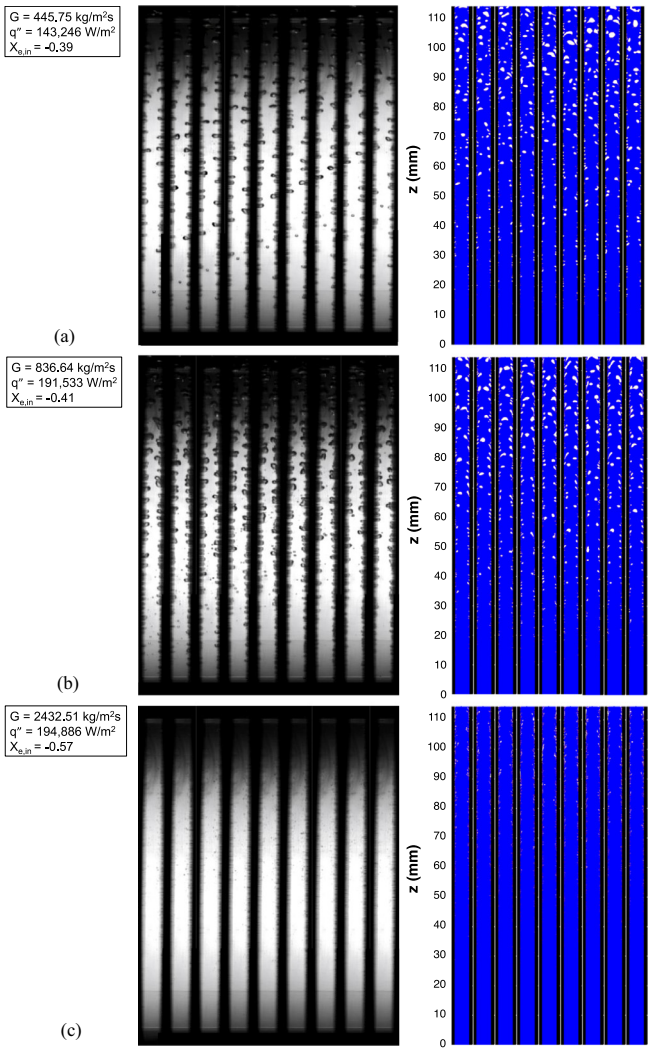

Fig. 5. Experimentally and computationally obtained sequential flow visualization images of entire heated portion of channel for (a) $G = 445.75$ kg/m^2 s, (b) $G = 836.64$ kg/m^2 s, and (c) $G = 2432.51$ kg/m^2 s.

Overall, experimental patterns of vapor bubble generation and evolution of interfacial behavior along the heated portion of the channel are predicted with good accuracy. The cases corresponding to the lowest and middle values of mass velocity, Fig. 5(a) and (b), show similar behavior along the channel, though bubbles for $G = 445.8$ kg/m^2 s are slightly larger than for $G = 2432.5$ kg/m^2 s. For both mass velocities, experiment and computation show the flow entering the heated portion of the channel as pure liquid, and bubbles begin to form along the heated walls at locations downstream from, but close to the inlet. Because of high inlet subcooling, bubbles are quite small at locations of bubble initiation. However, the bubbles grow axially because of both coalescence and diminishing condensation, the later resulting from gradual warming of the bulk liquid along the channel. Vapor bubbles in the downstream region are seen coalescing with incoming vapor,

and finally detaching from the wall to the liquid core. There is also appreciable deformation of vapor bubbles resulting from a variety of effects, including liquid drag, buoyancy, bubble collision, and bubble coalescence. Notice that, while vapor behavior along the walls appears in the computations predominantly symmetrical, there are some differences between the two walls, likely due to small-scale turbulence effects, as identical boundary conditions are assigned to both walls.

For the highest mass velocity of $G = 2432.5$ kg/m^2 s, Fig. 5(c) shows a vapor formation pattern distinctly different from that for the two lower mass velocities. Given both the high liquid inertia and ability of bulk liquid to better retain its subcooling along the channel, bubbles remain fairly small even toward the outlet. There is also a marked decrease in overall vapor void fraction. These conditions point to only a few cells in the computational domain satisfying saturation condition for phase change. This issue will be discussed again later by examining thermal boundary profiles across the channel.

To better understand the effects of mass velocity on interfacial behavior along the channel, axial variations of cross-section averaged vapor void fraction are examined. Fig. 6(a)–(c) compare predicted void fractions for $G = 445.8$, 836.6, and 2432.5 kg/m^2 s, respectively, with those measured experimentally and obtained from published correlations. Each plot shows void fractions corresponding to four axial measurement locations, with the entrance and exit locations purposely omitted, the former because of lack of observable vapor formation, and latter due to inability to distinguish bubble outlines from shadows in the experimental images. Calculation of void fraction from simulations is made by averaging 100 instantaneous results corresponding to 1.5 s of steady-state simulation time. Standard deviations for each set of 100 measurements corresponding to each case are also included in the plots, shown as error bars associated with each computed value of void fraction.

For the experimental data, a few images are carefully selected, with image segmentation conducted by Fuzzy C-means clustering [73] to identify bubble outlines. And calculation of the experimental void fraction is done through image processing and based on the assumption bubble shape is spherical, truncated hemispherical, or truncated ellipsoidal. Fig. 6(a)–(c) also include void fraction predictions based on empirical correlations by Zivi [74] and bases on the drift flux model [75]. In order to use these void fraction methods, vapor quality, x, should be computed first. Notice that x is different from thermodynamic equilibrium quality, x_e, especially for subcooled boiling, where x has finite positive value while x_e is negative. Vapor quality is obtained from experimental thermodynamic equilibrium quality according to a relation by Saha and Zuber, and Kroeger and Zuber [76,77],

$$x = \frac{x_e - x_d \exp(x_e/x_d - 1)}{1 - x_d \exp(x_e/x_d - 1)}, \tag{10}$$

where x_e is local thermodynamic equilibrium quality (obtained from a simple energy balance), and x_d is thermodynamic equilibrium quality at the point of net vapor generation (NVG). Based on analysis of video images, NVG points are seen at $z = 14.05$, 14.05 and 2.7 mm for $G = 445.8$, 836.6, and 2432.5 kg/m^2 s, respectively.

Fig. 6(a) and (b) show void fraction starts from a low value of ~1–2% at the first axial location and increases gradually. Notice that the measured void fraction begins to increase more rapidly around $z = 60$ mm, which is where large bubbles are observed in Fig. 5(a) and (b). Overall, the computed results match experiment quite well, but, expectedly, over-predict experiment by a small amount since the shape of vapor bubbles in 2D domain is treated as cylindrical rather than spherical. In addition, the empirical correlations provide somewhat different predictions, but fair agreement with both experiment and computations. However, the drift flux model provides relatively higher predictions for the intermediate mass velocity, Fig. 6(b), which is due to the fact that drift

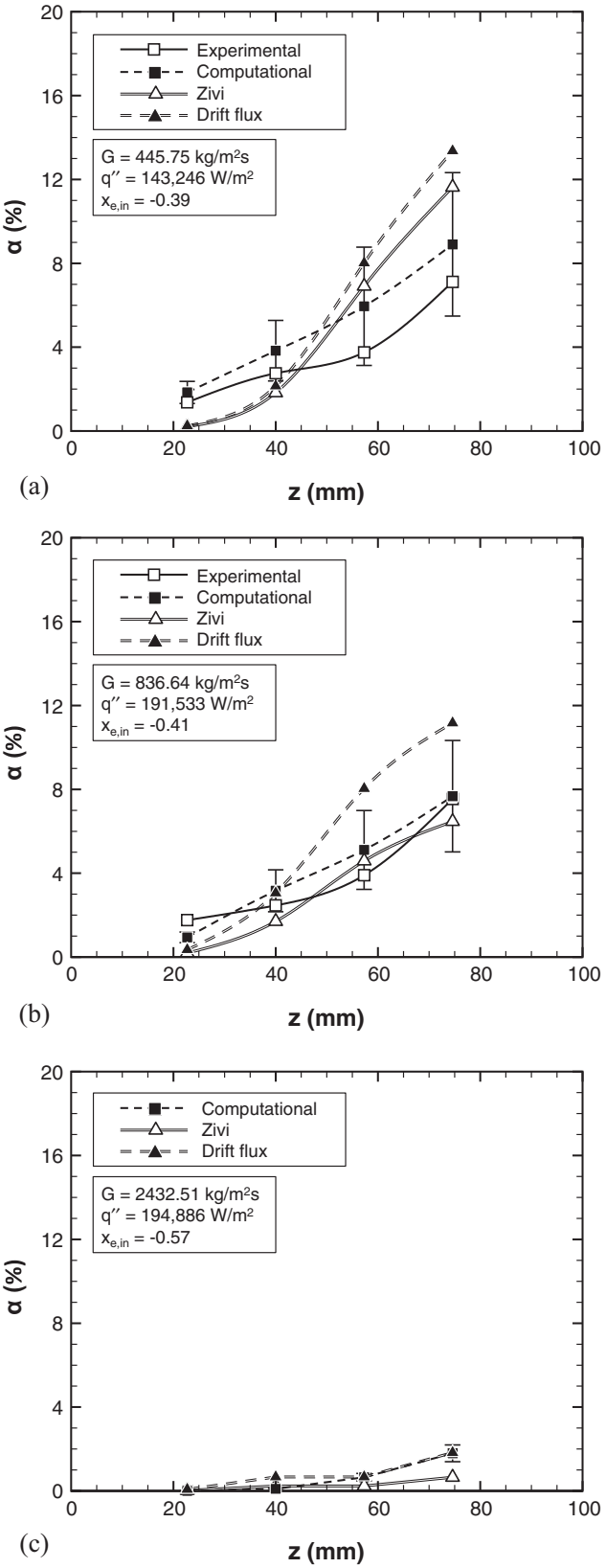

Fig. 6. Comparison of experimental and computed axial variations of cross-section averaged void fraction along with predictions based on prior empirical formulations for (a) $G = 421.59$ kg/m^2 s, (b) $G = 830.70$ kg/m^2 s, and (c) $G = 2435.41$ kg/m^2 s.

flux model is less than ideal for highly subcooled boiling conditions. Fig. 6(c) shows high mass velocity suppresses bubble growth appreciably, resulting in very small void fractions in the range of ~0–2%.

4.1.2. Void and velocity profiles across and along the channel

Also important to understanding interfacial behavior within the channel are distributions of void fraction and flow velocity across the channel. It is important here to emphasize the symmetries in both inlet velocity profile and heat flux applied to the two heated walls. This implies that any asymmetry captured by the simulations is the result of local vapor generation within the channel. Profile predictions are provided in Fig. 7(a) and (b). Fig. 7(a) shows plots for transverse void profile for each of the three mass velocities at different axial locations along the channel, while Fig. 7(b) provides corresponding plots for time-averaged velocity profile of the mixture; time-averages for both void fraction and velocity are achieved over a period of one second. Notice how the void fraction profiles resemble those typical of bubbly flow with a subcooled liquid core. It starts with zero distribution at the upstream location, meaning no vapor has yet been generated. This is followed at the second axial location with peak void in close proximity to the wall, in contrast with greatly reduced void near the centerline. This is indicative of a bubble layer residing in close proximity to the wall, with liquid occupying most of the channel core. For the lowest and middle mass velocities, Fig. 7(a) shows further penetration of the vapor layer towards the centerline at the third and fourth axial locations, which is the outcome of bubble growth and coalescence promoted by gradual warming of core liquid. There are important differences between the void distributions for the lowest and middle mass velocities on one hand and those for the highest mass velocity. For the highest mass velocity ($G = 2432.51$ kg/m^2 s), near-wall peaks in the void profile increase while maintaining zero value across much of the core, the latter is the result of greater sensible energy content in the subcooled liquid at high mass velocities. Confinement of the bubble layer to the wall region is also the result of greater liquid inertia for the highest mass velocity.

For the wall-normal velocity profiles, Fig. 7(b) shows fluid acceleration along the channel, which is the outcome of gradual axial increase in void fraction and reduction in mixture density. Notice for $G = 445.75$ and 836.64 kg/m^2 s how velocities at $z = 74.6$ mm are slightly higher near the wall compared to the core. This is the result of vapor accumulation near wall with the core velocity lagging in response to localized growth in void fraction. Eventually, the effect of the vapor generation is felt even within the core region at $z = 109.2$ mm because of migration of vapor bubbles towards the centerline. For the highest mass velocity ($G = 2432.51$ kg/m^2 s), however, miniscule void fraction precipitates little acceleration along the flow channel, evidenced by only minute axial changes in velocity profile.

Vapor growth, detachment, entrainment, and coalescence are innate features of bubbly flow boiling. Fig. 8(a)–(c) show, for $G = 445.8$, 836.6, and 2432.5 kg/m^2 s, respectively, enlargements of instantaneous vapor formation obtained from the simulations, along with plots for stream-wise and wall-normal velocities across the dashed planes indicated in each respective contour.

Fig. 8(a) depicts behavior at the moment of coalescence of vapor bubbles and formation of extended vapor ligament. The stream-wise velocity plot in Fig. 8(a) shows the vapor ligament, aided by buoyancy, associated with an appreciable increase in local velocity relative to surrounding liquid. Transverse velocity of the vapor ligament is positive, indicating tendency of the ligament to move toward the centerline. Fig. 8(b) captures one bubble detaching from the wall as well as a larger bubble entrained within the bulk liquid flow. Here too, bubbles are associated with higher axial velocity than surrounding liquid and a tendency to migrate towards the centerline. Both Fig. 8(a) and (b) show stream-wise velocity is an order of magnitude greater than transverse velocity, meaning z-momentum is much stronger than y-momentum and bubbles migrate towards the centerline at a comparatively slow rate. It is interesting to note that transverse velocity of liquid between the wall and detaching bubble is negative, which points to liquid replenishment of the wall. Turbulent mixing can enhance both bubble detachment and liquid replenishment. Notice how the cells occupied by liquid exist near wall even where temperature is equal to or slightly higher than saturation temperature. This can be explained by the fast fluctuations in cell temperature with each time step. The time-step used in this study is about 10^{-6} s, which is far too small to enable transformation from liquid to vapor numerically.

Fig. 8(c) elucidates local flow characteristics around an elongated bubble near the wall at the highest mass velocity. As discussed earlier, both vapor bubble formation and penetration into the core are suppressed at this high mass velocity because of high liquid inertia and high sensible heat content. No considerable fluctuation of z-velocity of the mixture is detected in the core region, and the z-velocity close to the wall shows elongated vapor obeying the no-slip condition, different from the other cases. Transverse velocity of vapor is negative, indicating the elongated vapor bubble is being squeezed towards the wall. One important distinction between the two lower mass velocities, Fig. 8(a) and (b), and the highest, Fig. 8(c), is a far greater (two orders of magnitude) ratio of axial to transverse velocity for the latter, evidence of inability of smaller bubbles to migrate away from the wall for the highest mass velocity.

Based on the local velocities profiles presented in Fig. 8(a)–(c), values of slip ratio, defined as vapor-to-liquid velocity ratio, are computed for the three mass velocities investigated. Fig. 9 shows computed slip ratios along with those predicted according to relations by Zivi [74] and Smith [78]. For the computed slip ratio, interfacial cells with volume fractions in the range of $0 < \alpha < 1$ are excluded from consideration, and only cells filled completely with liquid or vapor are used. The Zivi relation (also known as Zivi kinetic energy model 1) is based entirely on density ratio,

$$S = \frac{u_g}{u_f} = \left(\frac{\rho_f}{\rho_g}\right)^{1/3}, \tag{11}$$

while the Smith model is based on the assumption of separated flow with equal momentum fluxes in the two phases,

$$S = \frac{u_g}{u_f} = e + (1-e)\left[\frac{\left(\frac{\rho_f}{\rho_g}\right) + e\left(\frac{1-x}{x}\right)}{1 + e\left(\frac{1-x}{x}\right)}\right]^{1/2}, \tag{12}$$

where $e = 0.4$ and x represents vapor quality computed by Eq. (9).

Fig. 9 shows simulation results exhibit much closer agreement with predictions based on the Smith model than the Zivi model. However, even with the Smith model, there is some deviation from computed slip ratio for the highest mass velocity of $G = 2432.51$ kg/m^2 s, which can be explained by departure of flow regime for this mass velocity from the annular flow assumption of the Smith model.

4.2. Heat transfer characteristics in subcooled boiling

Fig. 10(a)–(c) show computed instantaneous temperature contours of both fluid and solid regions for $G = 445.8$, 836.6, and 2432.5 kg/m^2 s, respectively, with heat flux conditions corresponding to ~42–45% of CHF for each case. In these figures, regions of high temperature correspond to vapor and those of low temperature to liquid, while the liquid-vapor interfaces are maintained near saturation. As expected, operating conditions, vapor generation,

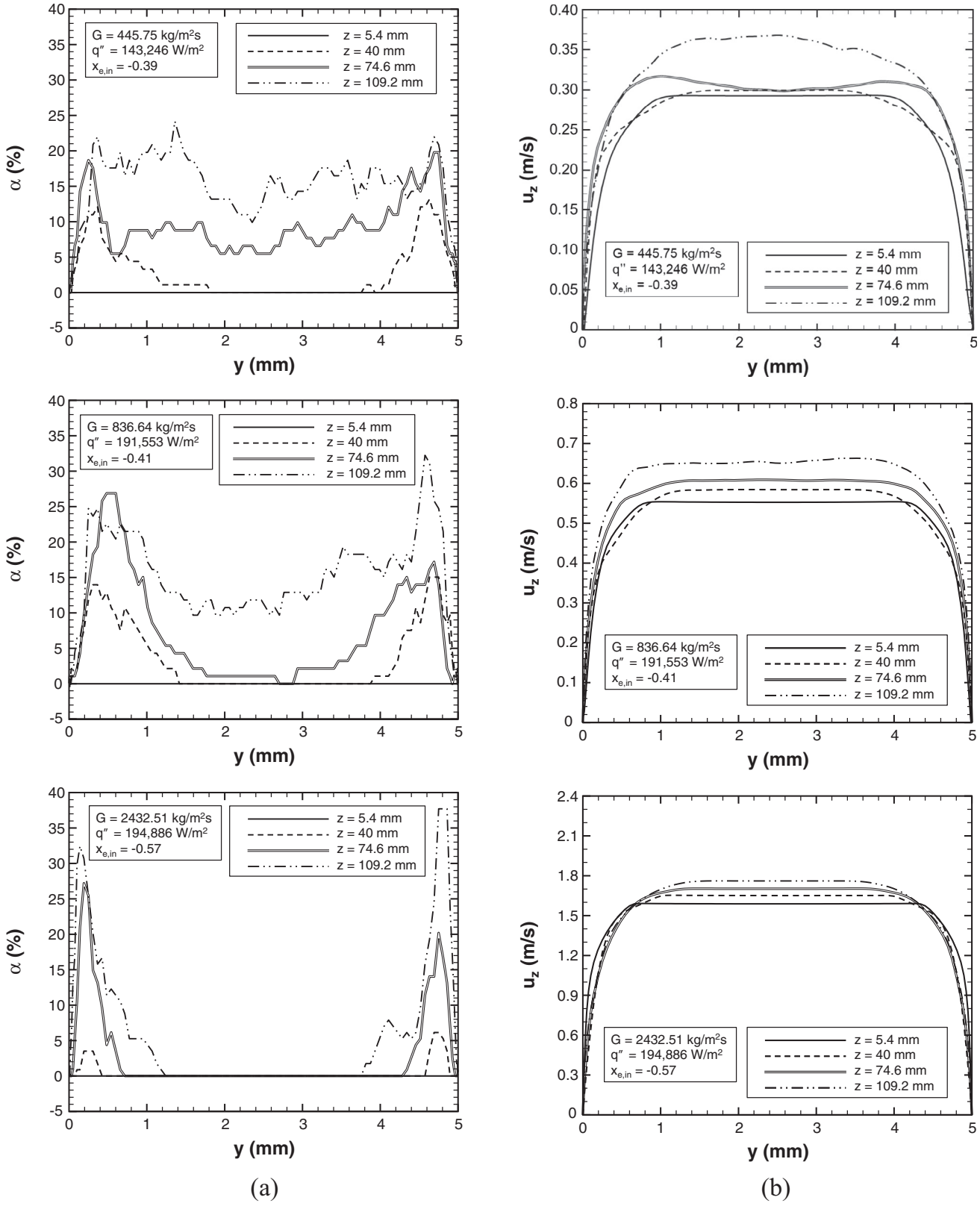

Fig. 7. Comparison of time-averaged transverse (a) void fraction and (b) stream-wise velocity profiles for three mass velocities and different axial locations.

and phase distribution significantly influence temperature profile within the channel, and the solid walls exhibit the expected axial temperature increase.

Fig. 10 shows heat dissipation for the lowest mass velocity of $G = 445.75\ \mathrm{kg/m^2\,s}$ in the entrance region dominated by single-phase liquid convection. With initiation of bubble nucleation, thermal boundary layer characteristics change, as heat from solid to fluid begins to be dissipated by nucleate boiling. As bubbles grow and detach from the wall, high temperature regions penetrate farther towards the channel centerline. In the downstream region,

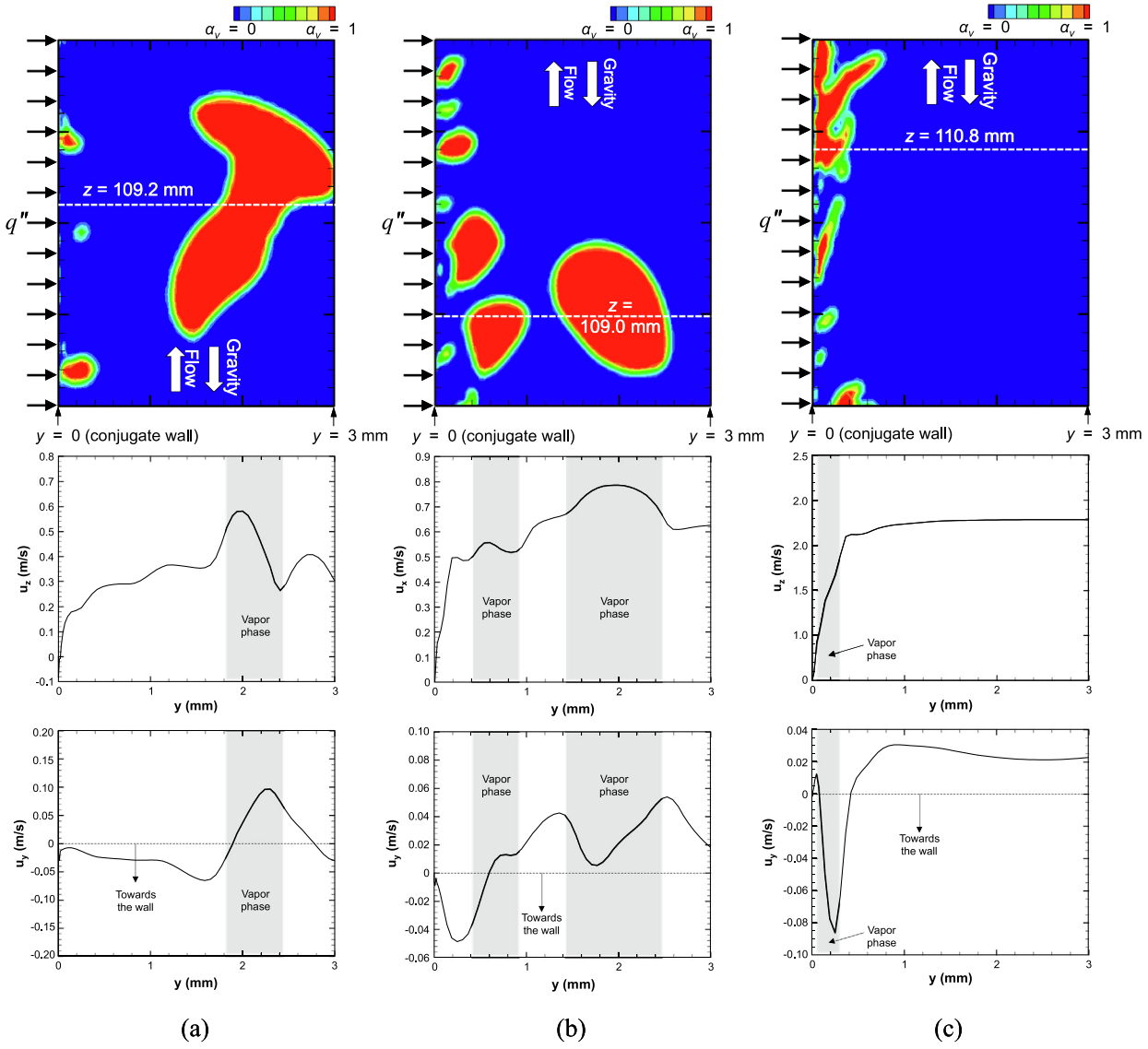

Fig. 8. Enlarged instantaneous vapor formation in downstream region and corresponding stream-wise and transverse velocity profiles for (a) $G = 445.75$ kg/m^2 s, $q'' = 143{,}246$ W/m^2, $x_{e,in} = -0.39$, (b) $G = 836.64$ kg/m^2 s, $q'' = 191{,}533$ W/m^2, $x_{e,in} = -0.41$, and (c) $G = 2432.51$ kg/m^2 s, $q'' = 194{,}886$ W/m^2, $x_{e,in} = -0.57$.

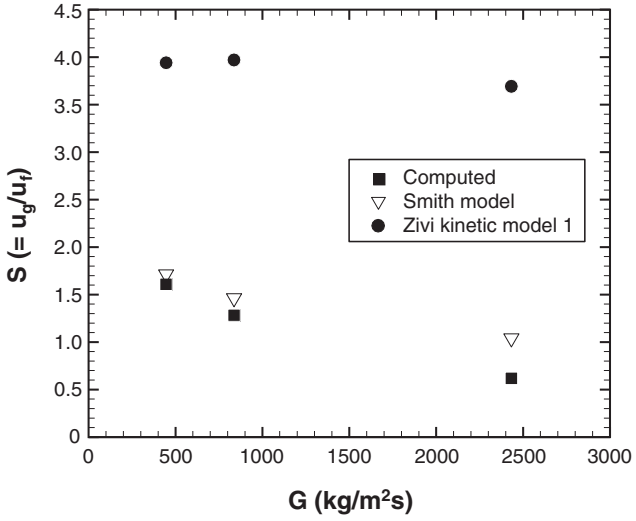

Fig. 9. Comparison of computed slip ratio to predictions of prior models for three different mass velocities.

heat is transferred mostly by nucleate boiling; large bubbles frequently detach from the wall and newly-generated vapor bubbles absorb thermal energy. A disordered temperature field downstream is clearly observed due to turbulent effects stemming from high mixing caused by motion of bubbles, indicating convective heat transfer is increased. Similar to the lowest mass velocity case, temperature field for the intermediate mass velocity of $G = 836.64$ kg/m^2 s in the entrance region is dominated by solid-liquid sensible heating, which is followed a short distance downstream by nucleate boiling. Here too, temperature field is fairly chaotic downstream, but slightly less so than with the lowest mass velocity because of reduced bubble detachment and penetration into the bulk liquid region. Temperature field for the highest mass velocity of $G = 2432.51$ kg/m^2 s is distinctly different for those for the two lower mass velocities. Here, a large upstream fraction of the channel is dominated by solid-liquid sensible heating, as core liquid is better able to sustain subcooled state, and measurable nucleate boiling and phase change are delayed farther downstream. Relatively high temperature regions are observed only near the wall where the vapor generation is confined.

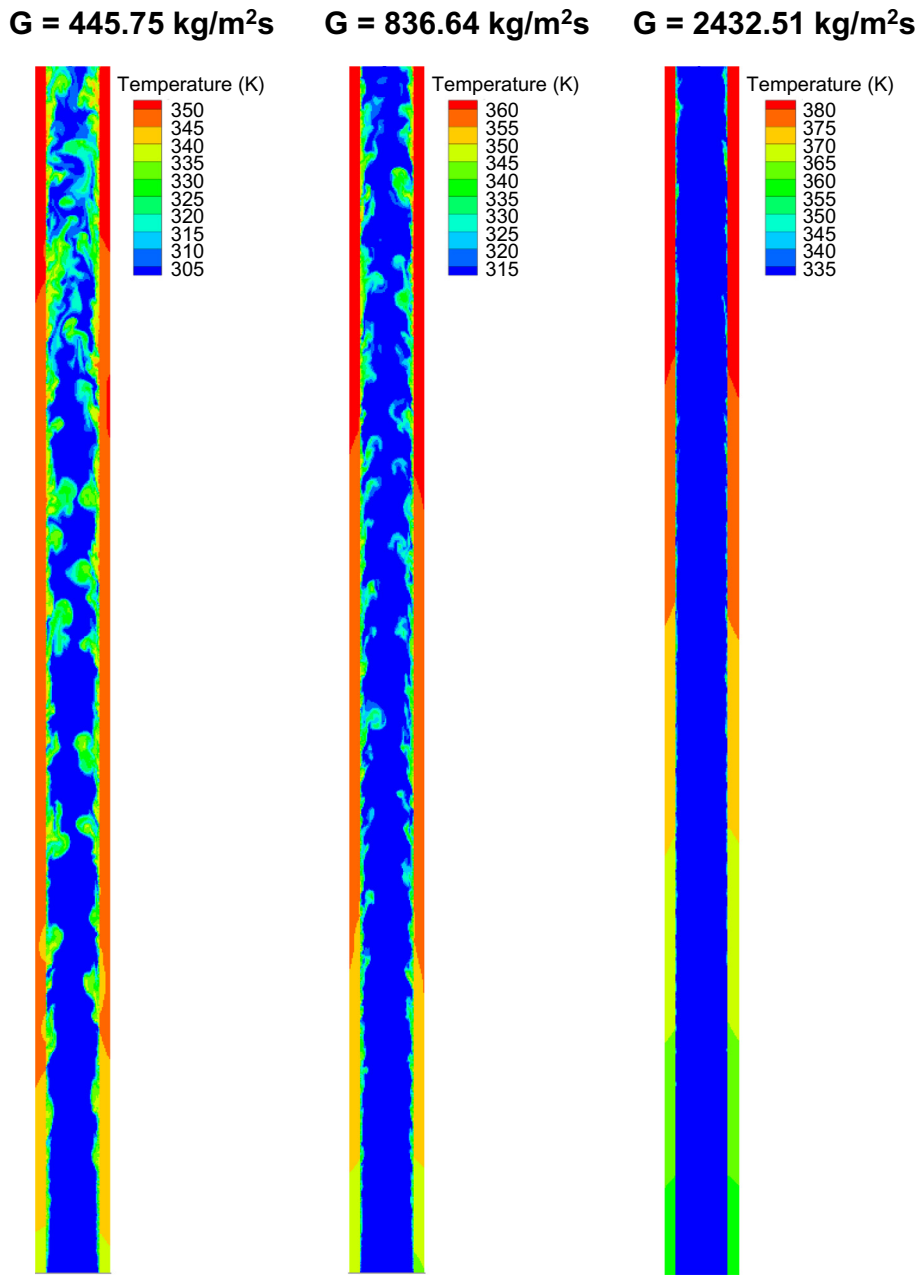

Fig. 10. Predicted temperature field in fluid and solid regions for entire heated portion of the channel at different mass velocities.

Accurate estimation of wall temperature is important to preventing thermal system failure, and allows adjustment of system parameters to improve performance. Fig. 11(a)–(c) compare predicted and measured wall temperatures along the channel for $G = 445.75$, 836.64, and 2432.51 kg/m^2 s, respectively. Here, predicted wall temperature is time-averaged over a period of one second of steady-state simulations. Notice that because temperature measurements are obtained in both walls, these plots include these measurements separately. For the lowest mass velocity, $G = 445.75$ kg/m^2 s, Fig. 11(a) shows wall temperature increases in the entrance region in response to axial liquid warming since this is where single-phase heat transfer is most appreciable. But within the nucleate boiling region, wall temperature is maintained fairly constant, between 345 and 350 K. Despite about a 7 K overprediction compared to the measurements, the model shows good accuracy along the entire heated portion of the channel. For the intermediate mass velocity of $G = 836.64$ kg/m^2 s, Fig. 11(b) shows axial variations of predicted wall temperature similar to those in Fig. 11(a), with reasonable accuracy in predicting the temperature data. However, the predictions in Fig. 11(c) for the highest mass velocity of $G = 836.64$ kg/m^2 s show appreciable departure from the data, which grows steadily along the channel. And, while predicted temperature increases monotonically in the axial direction, the data increase in the entrance region but decrease slightly thereafter. Reasons behind deviation of predictions from measurements will be addressed later.

Fig. 12(a)–(c) show axial variations of local heat transfer coefficient, h, with distance for $G = 445.75$, 836.64, and 2432.51 kg/m^2 s, respectively, and heat fluxes raging from ~42–45% of CHF. Like the wall temperatures, the predicted values of h are time-averaged over a period of one second of steady-state simulations. In addition, an area-weighted temperature for the fluid mixture is used

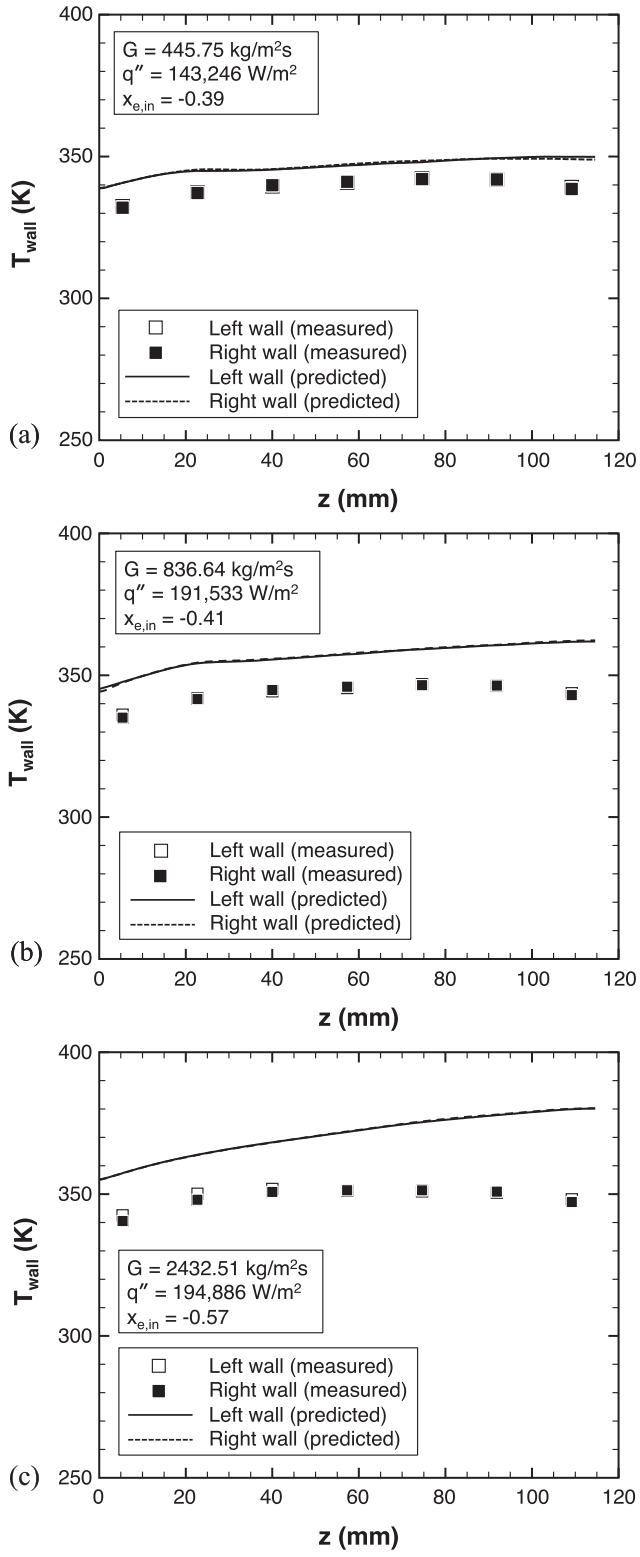

Fig. 11. Comparison of measured and predicted axial variations of wall temperatures for (a) $G = 445.75$ kg/m^2 s, (b) $G = 836.64$ kg/m^2 s, and (c) $G = 2432.51$ kg/m^2 s.

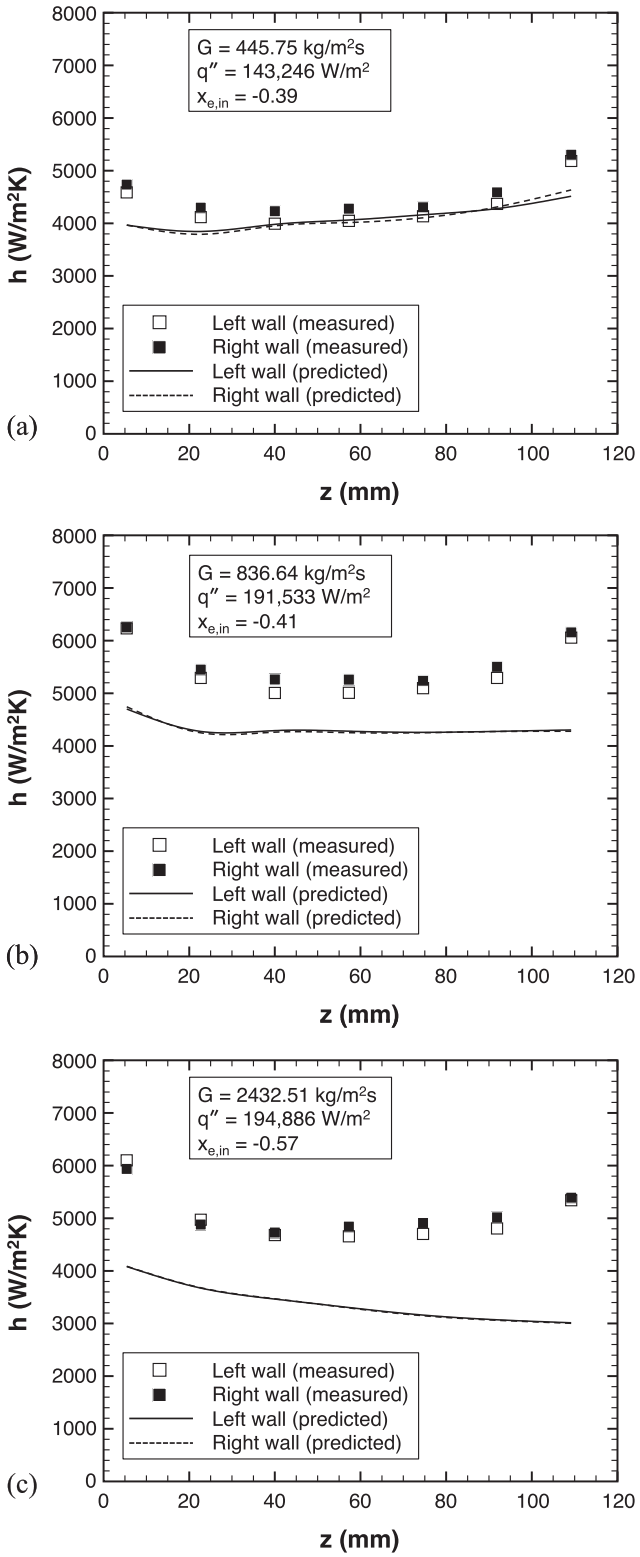

Fig. 12. Comparison of measured and predicted axial variations of local heat transfer coefficient for (a) $G = 445.75$ kg/m^2 s, (b) $G = 836.64$ kg/m^2 s, and (c) $G = 2432.51$ kg/m^2 s.

to compute temperature differences. Since it is difficult to measure fluid temperature experimentally at each axial measurement location, experimental fluid temperatures presented in Fig. 12(a)–(c) are calculated from a simple control-volume energy balance.

Overall, computed heat transfer coefficients under-predict experimental values to various degrees depending on mass velocity. The measured h decreases in the upstream region, becomes rather flat in the middle region, and increases again in the exit region. The upstream decline in measured h is attributed to thermal boundary layer development in predominantly liquid flow. On the other hand, the downstream increase in measured h is

the outcome of axial acceleration of the flow along the channel resulting from increased void fraction as discussed earlier in conjunction with Fig. 6. Notice that the acceleration is more pronounced for the lower two mass velocities, and are reflected by larger downstream increases in h compared to the highest mass velocity. Overall, the predicted h does reflect the inlet reduction in the heat transfer coefficient for all three mass velocities. Fig. 12(a) shows predictions for $G = 445.75$ kg/m^2 s are in good agreement with measurements, and capture both profile flattening in the middle region and downstream enhancement. Fig. 12(b) shows predictions for $G = 836.64$ kg/m^2 s do capture the inlet decrease in h and flat profile in the middle, but show the flat profile persisting to the outlet rather than capturing the downstream enhancement; the h values are also somewhat under-predicted by the simulations. Fig. 12(c) shows simulations for $G = 2432.51$ kg/m^2 s under-predict the measured values for the entire heated length and are not able to predict the measured middle flatness or downstream enhancement.

Overall, the computational model shows reasonable success in predicting wall temperatures and heat transfer coefficients, but with the deviation between predicted and measured values increasing with increasing mass velocity. One reason for these deviations is limitations of the 2D domain employed in the present simulations. Compared to the physical boiling process, the 2D approach cannot predict actual shape of bubbles. Instead, bubbles in 2D appear cylindrical or truncated cylindrical, as opposed to spherical or semi-spherical in 3D, resulting in less predicted area in contact with the liquid phase. In addition, 3D turbulence effects that undoubtedly influence fluid mixing and vapor bubble motion are not accounted for in the simulations. Another reason that is related to the use of 2D simulations is absence of shear stress produced by the adiabatic sidewalls. This shear stress becomes increasing more significant with increasing mass velocity, and its absence from computations may explain the higher deviations when predicting fluid flow and heat transfer parameters for the highest mass velocity of $G = 2432.51$ kg/m^2 s. Further, the VOF model solves a single momentum equation that does not account properly for drag or lift forces relating to bubble detachment.

Fig. 13(a)–(c) show variations of computed local time-averaged temperature profiles across the channel for $G = 445.75$, 836.64, and 2432.51 kg/m^2 s, respectively, corresponding to four axial locations. Here, time averaging is conducted over one second after reaching steady state. The area-weighted temperature average for the fluid mixture is computed as was done in Fig. 12(a)–(c). For all three cases, the thermal boundary layer is not fully developed at $z = 5.7$ mm, but gradually develops with distance. For the lowest flow rate of $G = 445.75$ kg/m^2 s, Fig. 13(a) shows the cross-section at $z = 5.7$ mm filled with mostly subcooled liquid at approximately $T = 301$ K, with a large temperature gradient near the walls. Moving along the channel, there are appreciable increases in core temperature and decreases in temperature gradient near the wall. After $z = 40.0$ mm, mixture temperature near the wall is superheated ($T_{sat} = 333.31$ K), and the superheated region becomes thicker with distance. At $z = 109.2$ mm, the thickness of the superheated region is around 200 μm. The downstream temperature profiles show some fluctuation, which is attributed to vapor bubbles with high temperature in the liquid core. For the intermediate mass velocity of $G = 836.64$ kg/m^2 s, Fig. 13(b) shows similar trends of mixture temperature across the channel, likely due to the flow regime being somewhat similar to that for the lowest mass velocity. However, the axial increase in core temperature is less significant and wall temperature gradients more pronounced compared to the lowest mass velocity. For $G = 2432.51$ kg/m^2 s, Fig. 13(c) shows temperature profile is flat in the core region for all four axial locations, indicating highly subcooled liquid is present along the entire heated region, and vapor bubbles are too small to drift into the core region. Considerable temperature gradient near the wall is observed, and this points to difficulty using equilibrium analysis when modeling subcooled flow boiling. Because of vapor accumulation near the wall in the downstream region, the fluid mixture is superheated to a maximum of 359 K (much higher than the saturation temperature of $T_{sat} = 342.5$ K). Near the exit ($z = 109.2$ mm), the superheated region for this high

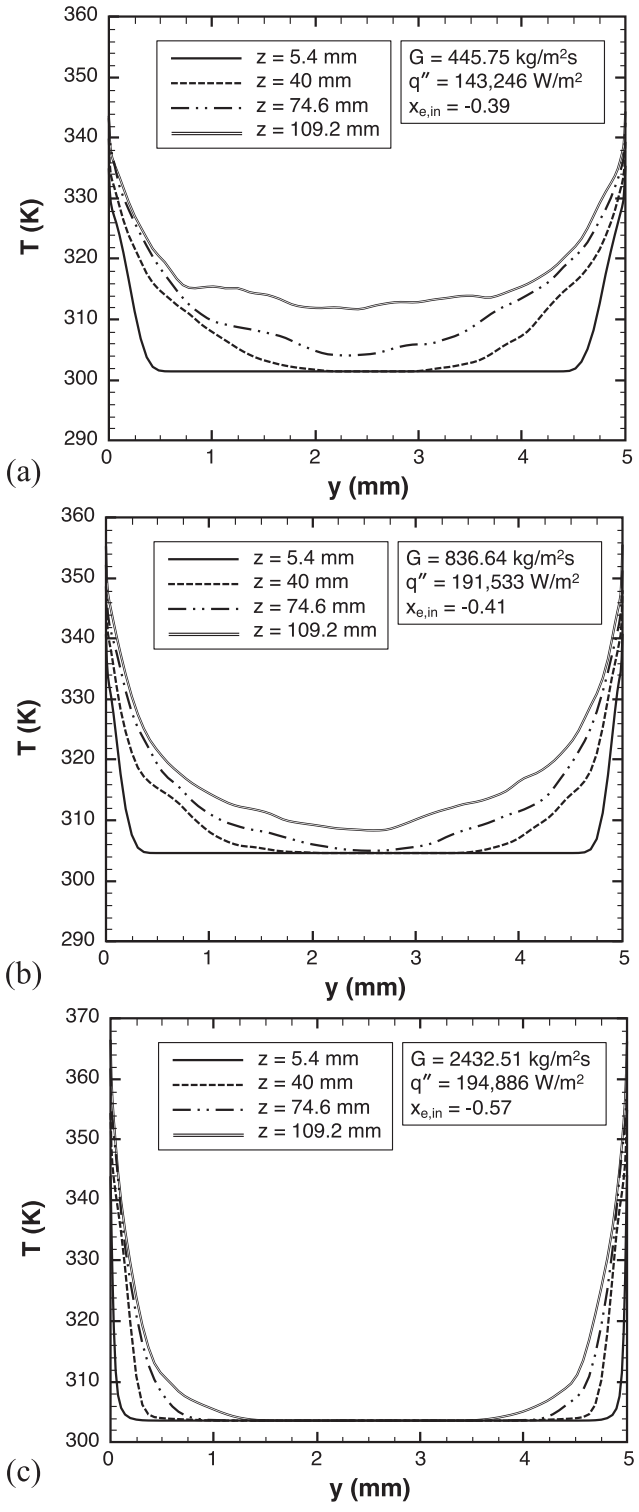

Fig. 13. Variations of computed fluid temperature profile across channel at four axial locations for (a) $G = 445.75$ kg/m^2 s, (b) $G = 836.64$ kg/m^2 s, and (c) $G = 2432.51$ kg/m^2 s.

mass velocity case is thinner by 100 μm compared to that of the lowest mass velocity.

4.3. Future work

Several methods are being adopted to predict fluid flow and heat transfer behavior of vapor-liquid system. Aside from computational methods, three other methods are commonly used: (1) theoretical models, few of which are available in the heat transfer literature, (2) semi-empirical models, which are based on theoretical mechanistic premises but fitted with empirical constants derived from experiments for closure, and (3) experimental correlations.

Today, thermal engineers rely almost exclusively on experimental correlations for both performance assessment and system design. Two important categories of correlations are (a) narrow range correlations and (b) 'universal correlations', the later being the method of choice where available. Universal correlations (see [37–39,79–83]) have benefitted greatly in recent years from studies amassing world databases for many fluids, and vary broad ranges of pressure, quality, mass velocity, and hydraulic diameter.

Looking ahead, computational work, like the one presented here, represents an important step towards achieving the ultimate goal of developing 3D codes that are experimentally validated, computationally efficient, and sufficiently robust for design purposes. Until such goal is reached, it is unlikely that the engineering community would transition from reliance on experimental correlations.

5. Conclusions

This study explored subcooled nucleate flow boiling of FC-72 for three different mass velocities with heat fluxes of ~42–45% of CHF applied to opposite heated walls of a rectangular channel in vertical upflow. Detailed presentations of both computational and experimental methods were provided. Predictions generated by 2D simulations incorporating multi-phase volume of fluid (VOF) model with an appropriate phase change model (Lee model) in ANSYS FLUENT were compared to experimental results. Computed results were also compared with predictions of prior correlations to provide basis for physicality of local results. Various phenomena that are difficult to measure experimentally were also examined, including void fraction, velocity profile, and local mixture temperature. Worthy findings from the present study are as follows:

(1) Mass transfer intensity factor r_i must be carefully set in the computational model for prediction of flow boiling, as it influences wall temperature and bubble formation at the wall. Very low r_i values yield a small amount of phase change, resulting in an increase in wall temperature. On the other hand, very high r_i values produce a vapor blanket at the wall inducing abnormally high wall temperature by blocking liquid replenishment of the wall. Both extreme values result in interfacial behavior along the channel vastly different from that observed experimentally using high speed video. A value of r_i = 10 is deemed optimum for the present combination of operating conditions and working fluid.

(2) Predicted flow patterns involving vapor generation, coalescence, detachment, and bubble deformation within the entire heated portion of the channel show good agreement with video images. Axial void fraction is numerically calculated and matches well experimental values as well as predictions of prior correlations. Detailed analysis of velocity and void fraction profiles across the channel demonstrate effectiveness of the computational model at providing detailed local information.

(3) Local mixture velocities around bubbles are investigated to assess ability of the computational scheme to provide accurate local predictions. Predicted local velocities show agreement with expected fluid behavior. Slip ratio is calculated for three different operating conditions and compared to correlations, showing good agreement with the Smith model except in the case with the highest mass velocity.

(4) Overall, the computational methodology presented here exhibits strong capability to represent the physical flow boiling processes observed experimentally. Accuracy of predictions decreases for high mass velocity, however, due largely to limitations associated with treating the nucleate flow boiling as a 2D process. Future work conducted using additional computational resources allowing for a 3D domain is likely to alleviate this shortcoming.

Conflict of interest

The authors declare that there are no conflicts of interest.

Acknowledgements

The authors are grateful for financial support provided by the National Aeronautics and Space Administration (NASA) under grant no. NNX17AK98G, and technical support of the NASA Glenn Research Center, Cleveland, Ohio. This work was also supported by NASA Space Technology Research Fellowship NNX15AP29H. The authors would also like to thank Aubrey Lokey for assistance gathering experimental data presented here.

Appendix A. Supplementary material

Supplementary data to this article can be found online at https://doi.org/10.1016/j.ijheatmasstransfer.2019.03.046.

References

[1] S. Ghosh, I. Calizo, D. Teweldebrhan, E.P. Pokatilov, D.L. Nika, A.A. Balandin, W. Bao, F. Miao, C.N. Lau, Extremely high thermal conductivity of graphene: prospects for thermal management applications in nanoelectronic circuits, Appl. Phys. Lett. 92 (2008) 151911.
[2] A. Rabiee, A. Atf, A computational fluid dynamics investigation of various nanofluids in a boiling flow field, Prog. Nucl. Energ. 95 (2017) 61–69.
[3] Y. Chen, M. Fiebig, N.K. Mitra, Heat transfer enhancement of a finned oval tube with punched longitudinal vortex generators in-line, Int. J. Heat Mass Transfer 41 (1998) 4151–4166.
[4] J.C. Han, Y.M. Zhang, C.P. Lee, Augmented heat transfer in square channels with parallel, crossed, and v-shaped angled ribs, J. Heat Transfer 113 (1991) 590–596.
[5] R.V. Rao, V. Patel, Multi-objective optimization of heat exchangers using a modified teaching-learning-based optimization algorithm, Appl. Math. Model. 37 (2013) 1147–1162.
[6] I. Mudawar, Two-phase microchannel heat sinks: theory, applications, and limitations, J. Electronic Packaging 133 (2011) 041002–41031.
[7] I. Mudawar, Recent advances in high-flux, two-phase thermal management, J. Thermal Sci. Eng. Appl. 5 (2013) 021012.
[8] L.S. Tong, Boundary-layer analysis of the flow boiling crisis, Int. J. Heat Mass Transfer 11 (1968) 1208–1211.
[9] W. Hebel, W. Detavernier, M. Decreton, A contribution to the hydrodynamics of boiling crisis in a forced flow of water, Nucl. Eng. Des. 64 (1981) 433–445.
[10] C.H. Lee, I. Mudawar, A mechanistic critical heat flux model for subcooled flow boiling based on local bulk flow conditions, Int. J. Heat Mass Transfer 14 (1988) 711–728.
[11] J.E. Galloway, I. Mudawar, CHF mechanism in flow boiling from a short heated wall-I. Examination of near-wall conditions with the aid of photomicrography and high-speed imaging, Int. J. Heat Mass Transfer 36 (1993) 2511–2526.
[12] J.E. Galloway, I. Mudawar, CHF mechanism in flow boiling from a short heated wall-II. Theoretical CHF model, Int. J. Heat Mass Transfer 36 (1993) 2527–2540.
[13] D.D. Hall, I. Mudawar, Critical heat flux (CHF) for water flow in tubes - I. Compilation and assessment of world CHF data, Int. J. Heat Mass Transfer 43 (2000) 2573–2604.
[14] I. Mudawar, T.M. Anderson, Parametric investigation into the effects of pressure, subcooling, surface augmentation and choice of coolant on pool

boiling in the design of cooling systems for high-power density chips, J. Electronic Packaging 112 (1990) 375–382.
[15] I.C. Bang, S.H. Chang, Boiling heat transfer performance and phenomena of Al2O3–water nano-fluids from a plain surface in a pool, Int. J. Heat Mass Transfer 48 (2005) 2407–2419.
[16] H.Y. Kim, Y.G. Kim, B.H. Kang, Enhancement of natural convection and pool boiling heat transfer via ultrasonic vibration, Int. J. Heat Mass Transfer 47 (2004) 2831–2840.
[17] J.A. Shmerler, I. Mudawar, Local evaporative heat transfer coefficient in turbulent free-falling liquid films, Int. J. Heat Mass Transfer 31 (1988) 731–742.
[18] T.H. Lyu, I. Mudawar, Statistical investigation of the relationship between interfacial waviness and sensible heat transfer to a falling liquid film, Int. J. Heat Mass Transfer 34 (1991) 1451–1464.
[19] S.M. Ghiaasiaan, Two-phase flow, boiling and condensation in conventional and miniature systems, Cambridge University Press, New York, 2008.
[20] W. Yu, D.M. France, M.W. Wambsganss, J.R. Hull, Two-phase pressure drop, boiling heat transfer, and critical heat flux to water in a small-diameter horizontal tube, Int. J. Multiphase Flow 28 (2002) 927–941.
[21] J. Lee, I. Mudawar, Fluid flow and heat transfer characteristics of low temperature two-phase micro-channel heat sinks – part 1: Experimental methods and flow visualization results, Int. J. Heat Mass Transfer 51 (2008) 4315–4326.
[22] J. Lee, I. Mudawar, Critical heat flux for subcooled flow boiling in micro-channel heat sinks, Int. J. Heat Mass Transfer 52 (2009) 3341–3352.
[23] W.P. Klinzing, J.C. Rozzi, I. Mudawar, Film and transition boiling correlations for quenching of hot surfaces with water sprays, J. Heat Treating 9 (1992) 91–103.
[24] M. Visaria, I. Mudawar, Effects of high subcooling on two-phase spray cooling and critical heat flux, Int. J. Heat Mass Transfer 51 (2008) 5269–5278.
[25] W.L. Cheng, F.Y. Han, Q.N. Liu, R. Zhao, H.L. Fan, Experimental and theoretical investigation of surface temperature non-uniformity of spray cooling, Energy 36 (2011) 249–257.
[26] I. Mudawar, D.C. Wadsworth, Critical heat flux from a simulated electronic chip to a confined rectangular impinging jet of dielectric liquid, Int. J. Heat Mass Transfer 34 (1991) 1465–1480.
[27] M. Monde, T. Inoue, Critical heat flux in saturated forced convective boiling on a heated disk with multiple impinging jets, J. Heat Transfer 113 (1991) 722–727.
[28] M.E. Johns, I. Mudawar, An ultra-high power two-phase jet-impingement avionic clamshell module, J. Electronic Packaging 118 (1996) 264–270.
[29] M.K. Sung, I. Mudawar, Single-phase hybrid micro-channel/jet impingement cooling, Int. J. Heat Mass Transfer 51 (2008) 4342–4352.
[30] T. Sato, H. Matsumura, On the conditions of incipient subcooled boiling and forced-convection, Bull. JSME 7 (1963) 392–398.
[31] E.J. Davis, G.H. Anderson, The incipience of nucleate boiling in forced convective flow, AIChE J. 12 (1966) 774–780.
[32] J.T. Rogers, M. Salcudean, Z. Abdullah, D. McLeod, D. Poirier, The onset of significant void in up-flow boiling of water at low pressure and velocities, Int. J. Heat Mass Transfer 30 (1987) 2247–2260.
[33] J.T. Rogers, J.H. Li, Prediction of the onset of significant void in flow boiling of water, J. Heat Transfer 116 (1994) 1049–1053.
[34] S.C. Lee, S.G. Bankoff, A comparison of predictive methods for the onset of significant void at low pressures in forced-convection subcooled boiling, KSME Int. J. 12 (1998) 504–513.
[35] R.M. Stoddard, A.M. Black, S.M. Ghiaasiaan, S.I. Abdel-Khalik, S.M. Jeter, M.F. Downing, Onset of flow instability and critical heat flux in this horizontal annuli, Exp. Thermal Fluid Sci. 26 (2002) 1–14.
[36] S.E. El-Morshedy, Predictive study of the onset of flow instability in narrow vertical rectangular channels under low pressure subcooled boiling, Nucl. Eng. Des. 244 (2012) 34–42.
[37] S.M. Kim, I. Mudawar, Universal approach to predicting two-phase frictional pressure drop for mini/micro-channel saturated flow boiling, Int. J. Heat Mass Transfer 58 (2013) 718–734.
[38] S.M. Kim, I. Mudawar, Review of databases and predictive methods for pressure drop in adiabatic, condensing and boiling mini/micro-channel flows, Int. J. Heat Mass Transfer 77 (2014) 74–97.
[39] S.M. Kim, I. Mudawar, Review of databases and predictive methods for heat transfer in condensing and boiling mini/micro-channel Flows, Int. J. Heat Mass Transfer 77 (2014) 627–652.
[40] C.R. Kharangate, I. Mudawar, Review of computational studies on boiling and condensation, Int. J. Heat Mass Transfer 108 (2017) 1164–1196.
[41] C. Kunkelmann, P. Stephan, CFD simulation of boiling flows using the Volume-of-Fluid Method within OpenFOAM, Num, Heat Transfer, Part A: Appl. 56 (2009) 631–646.
[42] M. Bahreini, A. Ramiar, A.A. Ranjbar, Numerical simulation of bubble behavior in subcooled flow boiling under velocity and temperature gradient, Nucl. Eng. Des. 293 (2015) 238–248.
[43] S.S. Rabha, V.V. Buwa, Volume-of-fluid (VOF) simulations of rise of single/multiple bubbles in sheared liquids, Chem. Eng. Sci. 65 (2010) 527–537.
[44] S. Osher, J.A. Sethian, Fronts propagating with curvature-dependent speed: algorithms based on Hamilton-Jacobi formulations, J. Comput. Phys. 79 (1988) 12–49.
[45] C.W. Hirt, B.D. Nichols, Volume of fluid (VOF) method for the dynamics of free boundaries, J. Comput. Phys. 39 (1981) 201–225.
[46] E. Da Riva, D. Del Col, Numerical simulation of laminar liquid film condensation in a horizontal circular minichannel, J. Heat Transfer 134 (2012) 051019–51028.
[47] S. Bortolin, E. Da Riva, D. Del Col, Condensation in a square minichannel: application of the VOF Method, Heat Transfer Eng. 35 (2014) 193–203.
[48] H. Lee, C.R. Kharangate, N. Mascarenhas, I. Park, I. Mudawar, Experimental and computational investigation of vertical downflow condensation, Int. J. Heat Mass Transfer 85 (2015) 865–879.
[49] C.R. Kharangate, H. Lee, I. Park, I. Mudawar, Experimental and computational investigation of vertical upflow condensation in a circular tube, Int. J. Heat Mass Transfer 95 (2016) 249–263.
[50] Z. Yang, X.F. Peng, P. Ye, Numerical and experimental investigation of two phase flow during boiling in a coiled tube, Int. J. Heat Mass Transfer 51 (2008) 1003–1016.
[51] M. Magnini, J.R. Thome, A CFD study of the parameters influencing heat transfer in microchannel slug flow boiling, Int. J. Thermal Sci. 110 (2016) 119–136.
[52] M. Bahreini, A. Ramiar, A.A. Ranjbar, Numerical simulation of subcooled flow boiling under conjugate heat transfer and microgravity condition in a vertical mini channel, Appl. Thermal Eng. 113 (2017) 170–185.
[53] D. Lorenzini, Y.K. Joshi, Computational fluid dynamics modeling of flow boiling in microchannels with nonuniform heat flux, J. Heat Transfer 140 (2018) 011501–11511.
[54] Y.K. Prajapati, M. Pathak, M.K. Khan, Numerical investigation of subcooled flow boiling in segmented finned microchannels, Int. Comm. Heat Mass Transfer 86 (2017) 215–221.
[55] C. Konishi, I. Mudawar, Review of flow boiling and critical heat flux in microgravity, Int. J. Heat Mass Transfer 80 (2015) 469–493.
[56] I. Mudawar, Flow boiling and flow condensation in reduced gravity, Advances Heat Transfer 49 (2017) 225–306.
[57] T.C. Willingham, I. Mudawar, Forced-convection boiling and critical heat flux from a linear array of discrete heat sources, Int. J. Heat Mass Transfer 35 (1992) 2879–2890.
[58] C.O. Gersey, I. Mudawar, Effects of heater length and orientation on the trigger mechanism for near-saturated flow boiling CHF - I. Photographic and statistical characterization of the near-wall interfacial features, Int. J. Heat Mass Transfer 38 (1995) 629–642.
[59] C.O. Gersey, I. Mudawar, Effects of heater length and orientation on the trigger mechanism for near-saturated flow boiling CHF - II. CHF model, Int. J. Heat Mass Transfer 38 (1995) 643–654.
[60] J.C. Sturgis, I. Mudawar, Critical heat flux in a long, rectangular channel subjected to one-sided heating – I. Flow visualization, Int. J. Heat Mass Transfer 42 (1999) 1835–1847.
[61] J.C. Sturgis, I. Mudawar, Critical heat flux in a long, rectangular channel subjected to one-sided heating - II. Analysis of CHF data, Int. J. Heat Mass Transfer 42 (1999) 1849–1862.
[62] H. Zhang, I. Mudawar, M.M. Hasan, Experimental assessment of the effects of body force, surface tension force, and inertia on flow boiling CHF, Int. J. Heat Mass Transfer 45 (2002) 4079–4095.
[63] H. Zhang, I. Mudawar, M.M. Hasan, Experimental and theoretical study of orientation effects on flow boiling CHF, Int. J. Heat Mass Transfer 45 (2002) 4463–4478.
[64] H. Zhang, I. Mudawar, M.M. Hasan, Flow boiling CHF in microgravity, Int. J. Heat Mass Transfer 48 (2005) 3107–3118.
[65] C.R. Kharangate, C. Konishi, I. Mudawar, Consolidated methodology to predicting flow boiling critical heat flux for inclined channels in Earth gravity and for microgravity, Int. J. Heat Mass Transfer 92 (2016) 467–482.
[66] L.E. O'Neill, I. Mudawar, M.M. Hasan, H.K. Nahra, R. Balasubramaniam, N.R. Hall, A. Lokey, J.R. Mackey, Experimental investigation into the impact of density wave oscillations on flow boiling system dynamic behavior and stability, Int. J. Heat Mass Transfer 120 (2018) 144–166.
[67] ANSYS FLUENT Theory Guide, ANSYS Inc., Canonsburg, PA, 2009.
[68] J.U. Brackbill, D.B. Kothe, C. Zemach, A continuum method for modeling surface tension, J. Comput. Phys. 100 (1992) 335–354.
[69] ANSYS ICEM CFD User's Manual, ANSYS Inc., Canonsburg, PA, 2009.
[70] R.W. Schrage, A theoretical study of interphase mass transfer, Columbia University Press, New York, 1953.
[71] I. Tanasawa, Advances in condensation heat transfer, Advances Heat Transfer 21 (1991) 55–139.
[72] W.H. Lee, Pressure iteration scheme for two-phase flow modeling, Multi-Phase Transport: Fundamentals, Reactor Safety, Appl. 1 (1980) 407–431.
[73] J.C. Bezdek, R. Ehrlich, W. Full, FCM: The fuzzy c-means clustering algorithm, Comput. Geosci. 10 (1984) 191–203.
[74] S.M. Zivi, Estimation of steady-state steam void-fraction by means of the principle of minimum entropy production, J. Heat Transfer 86 (1964) 247–251.
[75] N. Zuber, J.A. Findlay, Average volumetric concentration in two-phase flow systems, J. Heat Transfer 87 (1965) 453–468.
[76] P. Saha, N. Zuber, Point of net vapor generation and vapor void fraction in subcooled boiling, in: Proc. Fifth Int. Heat Transfer Conf. 4, Tokyo, Japan, 1974, pp. 175–179.
[77] P.G. Kroeger, N. Zuber, An analysis of the effects of various parameters on the average void fractions in subcooled boiling, Int. J. Heat Mass Transfer 11 (1968) 211–233.
[78] S.L. Smith, Void fractions in two-phase flow: a correlation based upon an equal velocity head model, Proc. Inst. Mech. Eng. 184 (1969) 647–664.

[79] S.M. Kim, I. Mudawar, Universal approach to predicting two-phase frictional pressure drop for adiabatic and condensing mini/micro-channel flows, Int. J. Heat Mass Transfer 55 (2012) 3246–3261.
[80] S.M. Kim, I. Mudawar, Universal approach to predicting heat transfer coefficient for condensing mini/micro-channel flows, Int. J. Heat Mass Transfer 56 (2013) 238–250.
[81] S.M. Kim, I. Mudawar, Universal approach to predicting saturated flow boiling heat transfer in mini/micro-channels part I. Dryout incipience quality, Int. J. Heat Mass Transfer 64 (2013) 1226–1238.
[82] S.M. Kim, I. Mudawar, Universal approach to predicting saturated flow boiling heat transfer in mini/micro-channels part II. Two-phase heat transfer coefficient, Int. J. Heat Mass Transfer 64 (2013) 1239–1256.
[83] S.M. Kim, I. Mudawar, Review of two-phase critical flow models and investigation of the relationship between choking, premature CHF, and CHF in micro-channel heat sinks, Int. J. Heat Mass Transfer 87 (2015) 497–511.